This article may be downloaded for personal use only. Any other use requires prior permission of the author and AIP Publishing. This article appeared in Zengshun Chen, Tengda Guan, Likai Zhang, Sunwei Li, Bubryur Kim, Yemeng Xu, Yunfei Fu, Cruz Y. Li; Flow interference investigation of multi-square prisms under fluid–structure interaction. II. Flow field phenomenology of side-by-side square prisms. Physics of Fluids 1 July 2024; 36 (7): 075138 and may be found at https://doi.org/10.1063/5.0210021.

Physics of Fluids

RESEARCH ARTICLE | JULY 11 2024

Flow interference investigation of multi-square prisms under fluid–structure interaction. II. Flow field phenomenology of side-by-side square prisms

Special Collection: Flow and Civil Structures

Zengshun Chen (陈增顺); Tengda Guan (关腾达); Likai Zhang (张利凯); Sunwei Li (李孙伟); Bubryur Kim; Yemeng Xu (许叶萌); Yunfei Fu (付云飞); Cruz Y. Li (李雨桐)

Check for updates

Physics of Fluids 36, 075138 (2024)
https://doi.org/10.1063/5.0210021

View Online
Export Citation

Articles You May Be Interested In

The flow interference investigation of multi-square prisms under fluid–structure interaction. I. Proximal wake characteristics of tandem square prisms

Physics of Fluids (July 2024)

Fluid–structure interaction on vibrating square prisms considering interference effects

Physics of Fluids (December 2023)

Characteristics of aerodynamic interference and flow phenomenology around inclined square prisms

Physics of Fluids (December 2023)

28 November 2025 03:08:21

AIP Publishing

AIP Publishing
Physics of Fluids
Special Topics Open for Submissions
Learn More

Physics of Fluids ARTICLE pubs.aip.org/aip/pof

Flow interference investigation of multi-square prisms under fluid–structure interaction. II. Flow field phenomenology of side-by-side square prisms

Cite as: Phys. Fluids **36**, 075138 (2024); doi: 10.1063/5.0210021
Submitted: 25 March 2024 · Accepted: 16 June 2024 ·
Published Online: 11 July 2024

View Online Export Citation CrossMark

Zengshun Chen (陈增顺),[1,a)] Tengda Guan (关腾达),[1,b)] Likai Zhang (张利凯),[1,c)] Sunwei Li (李孙伟),[2,d)] Bubryur Kim,[3,e)] Yemeng Xu (许叶萌),[1,f)] Yunfei Fu (付云飞),[4,g)] and Cruz Y. Li (李雨桐)[1,h)]

AFFILIATIONS

[1]School of Civil Engineering, Chongqing University, Chongqing 400045, China
[2]Shenzhen International Graduate School, Tsinghua University, Shenzhen 518055, China
[3]Department of Robot and Smart System Engineering, Kyungpook National University, 80 Daehak-ro, Buk-gu, Daegu 41566, South Korea
[4]Department of Building Environment and Energy Engineering, The Hong Kong Polytechnic University, Hung Hom, Kowloon, Hong Kong, China

Note: This paper is part of the special topic, Flow and Civil Structures.
[a)]**Electronic mail:** zengshunchen@cqu.edu.cn
[b)]**Electronic mail:** 202216131298t@stu.cqu.edu.cn
[c)]**Author to whom correspondence should be addressed:** zhanglikai@cqu.edu.cn
[d)]**Electronic mail:** li.sunwei@sz.tsinghua.edu.cn
[e)]**Electronic mail:** brkim@knu.ac.kr
[f)]**Electronic mail:** xu.ym@cqu.edu.cn
[g)]**Electronic mail:** yfuar@connect.ust.hk
[h)]**Electronic mail:** yliht@connect.ust.hk

28 November 2025 03:08:21

ABSTRACT

The current research primarily focuses on interference effects in rigid structures, with the omission of the feedback impact of structural vibration on the flow field preventing the disclosure of the intrinsic mechanisms behind interference effects. Therefore, this study analyzed the aerodynamic characteristics and flow field phenomena of the finite-length side-by-side square prisms under vibration through the large eddy simulation, unveiling the flow field morphology and disturbance mechanisms. The results show that the three-dimensional effect of the side-by-side square prisms effectively suppresses the deflection of the gap flow. Structural vibration increases the curvature of the shear layers on both sides of the interfering structure, weakens its end effect, and destroys the integrity of the axial vortex in the wake region. With the increase in the spacing between the side-by-side square prisms, the "narrow pipe effect" is weakened, the flow acceleration is relatively slowed down, and interference of the vortices in the wake region is weakened. In addition, some typical flow field phenomena are observed, such as gap flow instability, coupled vortex street, interaction of wakes, and different flow regimes. This study is of great significance for understanding mechanisms of the flow interference around the finite-length side-by-side square prisms under fluid–structure interaction.

Published under an exclusive license by AIP Publishing. https://doi.org/10.1063/5.0210021

NOMENCLATAURE

Latin letter

C_p	The mean pressure coefficient
C_s	The Smagorinsky constant
D	The edge length of the square structure
H	The height of the square structure
I_u	Turbulence intensity at x-direction
I_w	Turbulence intensity at z-direction
I_{ref}	Turbulence intensity at the reference height
I_v	Turbulence intensity at y-direction

Published under an exclusive license by AIP Publishing

L_u	Turbulent integral scale at x-direction
L_w	Turbulent integral scale at z-direction
L_v	Turbulent integral scale at y- direction
t^*	Dimensionless time step
U	Wind profile
U_r	The velocity at the reference height
$y_{\max}$	The maximum displacement
z	Structural height
z_{ref}	The reference height

Greek letters

α	Surface roughness index
$\Delta x_{\min}$	Thickness of the first layer of the boundary layer
Δt	The time step
μ	The fluid dynamic viscosity coefficient
μ_{sgs}	The sub-grid viscosity
σ_u	The root mean square of x-direction velocity
σ_v	The root mean square of y-direction velocity
σ_w	The root mean square of z-direction velocity

I. INTRODUCTION

Fluid–structure interaction (FSI) is a multidisciplinary research field involving the complex multi-physics coupling between fluid and structures. In FSI, the interaction between the fluid and the structure commonly leads to changes in the overall behavior of the system, exhibiting highly nonlinear and complex dynamic characteristics. This is particularly common in fields such as aerospace,[1] marine engineering,[2] and wind engineering.[3] Flow-induced vibration (FIV),[4–7] a typical issue of FSI, refers to the phenomenon that occurs when fluid flows through a square structure, flow separation, the formation of Karman vortex streets, and other phenomena around the structure. This results in periodic vibrations of the structure, triggering a significant increase in the unsteady aerodynamic force on the surface of the structure, leading to its deformation or damage.[8–10] Therefore, revealing the intrinsic mechanism of square structures under FSI is of great significance for accurately assessing structural safety.

Currently, the flow around a single square prism has been extensively studied.[11–14] However, in practical engineering applications, structures often exist in clusters. Compared with an isolated square prism, multi-square prism systems are more susceptible to the influence of various interference factors. These interference factors may cause changes in the flow field, thereby affecting the dynamic behavior of the entire system.[15–17] Side-by-side square prisms are a typical model for studying aerodynamic interference, which can reveal the FSI mechanism and aerodynamic interference effect of multi-square prisms. Research on side-by-side square prisms studies can be roughly divided into three categories: (1) the rigid model of infinite-length side-by-side square prisms, (2) the vibration model of infinite-length side-by-side square prisms under FSI, and (3) the rigid model of finite-length side-by-side square prisms.

For the rigid model of infinite-length side-by-side square prisms, to clarify their interference effects and mechanisms, numerous scholars have conducted a substantial amount of experimental studies and numerical simulations. For instance, Sau *et al.*[18] conducted numerical simulations to study the evolution of the vortex structure in the wake region of side-by-side square prisms at a Reynolds number of 100 and the flow separation patterns under different spacing ratios. It was found that the flow under different spacing ratios exhibits phase synchronization, symmetry, and stability characteristics. Subsequently, Yen and Liu[19] studied the boundary layer flow characteristics of side-by-side square prisms under different Reynolds numbers and spacing ratios. The smoke-wire scheme was used to visualize the flow structure, which was divided into three modes: single mode, gap-flow mode, and couple vortex-shedding. Simultaneously, a pressure transducer and a hot-wire anemometer were used to measure the pressure distribution, drag coefficient, and vortex shedding frequency on the surface of the square prisms. The results showed that the drag coefficient and Strouhal number were the lowest in the gap-flow mode. Alam *et al.*[20] and Lee *et al.*[21] utilized particle imaging velocimetry(PIV) to study the flow structure of side-by-side square prisms, conducting experimental measurements and numerical simulations at different spacing ratios. It was found that there are four different flow regimes for side-by-side square prisms, namely, the single-body regime, the two-frequency regime, the transition regime, and the coupled vortex street (CVS) regime. Then, the transition mechanism and characteristic parameters were revealed. Alam and Zhou[22] analyzed the special biased flow phenomenon of side-by-side square prisms at small spacing ratios. The flow characteristics under different spacing ratios were revealed, including gap vortices, flow switch, stability, and merging of two streets into one. The reasons for the gap flow bias were discussed, such as the mechanism of the merging of two wakes and the factors that trigger the switching of flow modes. Mizushima and Hatsuda[23] used stability analysis and numerical simulation to study the nonlinear interaction between symmetric and antisymmetric perturbation modes when the spacing ratio of the side-by-side square prisms was close to the critical value. The results showed that three equilibrium solutions appear near this critical value: a mixed-mode solution, symmetric and antisymmetric single-mode solutions. Among them, the mixed-mode solution is an asymmetric flow composed of the superposition of finite amplitudes of two perturbation modes, while the single-mode solution is a symmetric or asymmetric flow formed by one perturbation mode dominating. However, the aforementioned studies mainly focus on the analysis of rigid models of side-by-side square prisms. Ignoring the mutual coupling between fluid and structure can significantly impact the safety assessment of side-by-side square prisms.

Many researchers study the vibration model of infinite-length side-by-side square prisms under FSI, analyzing the aerodynamic characteristics and flow field phenomena. For example, Lu *et al.*[24] examined the effects of factors such as the spacing ratio, vibration frequency, and vibration amplitude on the mean and fluctuating drag coefficient of side-by-side square prisms. Meanwhile, the flow field characteristics, such as the vortex shedding frequency, vortex structure, and pressure correlation, were also discussed. Liu and Jaiman[25] analyzed side-by-side cylinders under different spacing ratios, Reynolds numbers, and reduced wind speeds. The results showed that the gap flow affects the vortex-induced vibration of the structure, narrowing the lock-in region. Moreover, vortex-induced vibration also affects the gap flow, causing the gap flow to deflect toward the vibrating cylinder within the lock-in region. Guan *et al.*[26] further investigated the side-by-side square prisms under FSI and analyzed the influence of different spacing ratios and reduced wind speeds on the flow field and vibration characteristics. The results indicated that the square cylinder under vibration exhibits vortex synchronization, transitional kink, and

28 November 2025 03:08:21

Published under an exclusive license by AIP Publishing

galloping phenomena, while the square prism under the combined vibration does not exhibit vortex synchronization. Kim and Alam[27] conducted the wind tunnel experiment to study the flow-induced vibration characteristics of side-by-side prisms. According to the vibration amplitude and phase difference, the flow-induced vibration was divided into four patterns: symmetric vibration, antiphase vibration, asymmetric vibration, and single-cylinder vibration. Xu *et al.*[28] simulated the flow-induced vibration phenomenon of two elastically mounted side-by-side prisms. The amplitude response, frequency response, trajectory, and flow field characteristics were analyzed, and six different wake patterns were identified based on the flow field visualization results. However, the above literature primarily focuses on the idealized infinitely length side-by-side square prisms, ignoring the three-dimensional effect of the prisms. This approach fails to effectively analyze the evolution and stability of the vortex structure in the wake region of prisms.

The rigid model of finite-length side-by-side square prisms has an obvious three-dimensional effect, which substantially impacts the formation and evolution of the vortex structure in the wake region. Numerous scholars have carried out relevant research on it. For example, Sohankar *et al.*[29] conducted an experimental investigation on the finite-length side-by-side square prisms, finding the four different flow modes, which are the asymmetric flow, antiphase shedding flow, leading edge separated flow, and wedge flow. It is shown that the finite length of the square prism leads to the formation of the tip vortex at the free end and the base vortex at the bottom, making the wake flow more complex and three dimensional. Subsequently, Sohankar *et al.*[30] employed the large eddy simulation to study the wake dynamics of side-by-side finite-length square prisms with different spacing ratios categorizing them into two main flow modes: biased/flip-flop flow ($S/d = 2$) and antiphase coupled vortex shedding flow ($S/d \geq 3$). Zdravkovich[31] carried out an experimental investigation to study the pressure distribution and aerodynamic coefficients of finite-length side-by-side prisms. The study found that there is also a bistable bias flow phenomenon in the finite-length side-by-side prism, where the flow between the two prisms alternately deflects to each side, resulting in different aerodynamic loads on the prisms. Bhamitipadi Suresh *et al.*[32] investigated the wake characteristics and aerodynamic characteristics of finite-length side-by-side square prisms under turbulent boundary layer inflow using PIV and analyzed the effects of different spacing ratios (T/d) on the mean and unsteady flow fields. The results showed that reducing the spacing ratio can effectively delay the wake recovery and suppress the downwash and upwash flow of the free end and base of the square prism. The mean lift coefficient near the top decreases with the increase in the spacing ratio, while the mean drag coefficient remains unchanged. Park and Lee[33] experimentally measured the wake velocity, the mean pressure distribution and flow field phenomena of finite-length side-by-side square prisms with different spacing ratios. The results showed that the increase in the spacing ratio leads to an increase in the vortex shedding frequency and Strouhal number. Additionally, a strong downwash flow is generated near the free end of the finite-length prisms, forming a pair of counter-rotating vortices.

For a rigid model of finite-length side-by-side square prisms, the main focus is on the three-dimensional effect, which reveals the formation of downwash and upwash flows at the free end and base, as well as the formation of vortex structures in the wake. However, the mutual coupling between fluid and structure is ignored, leading to discrepancies in the flow field morphology and aerodynamic characteristics compared to real situations. In light of this, this study conducts research on the finite-length side-by-side square prisms under FSI. Through large eddy simulation, the flow field changes of the side-by-side square prisms under vibration are studied, and the mean pressure coefficient, time-averaged flow field, spanwise instantaneous vorticity, and instantaneous vortex structure of the wake are analyzed, revealing the aerodynamic characteristics and flow field morphology. In summary, the primary objective of this study aims to (1) understand the fundamental behavior of the wake behind finite-length side-by-side square prisms; (2) investigate the effects of gap spacing and vibration on the wake morphology (such as changes in gap flow); and (3) establish the relationship between the aerodynamic characteristics and flow field characteristics of finite-length side-by-side square prisms. The study is divided into five sections: Sec. I introduces the research background. Section II describes numerical simulation setting. Section III presents validation and aerodynamic characteristics. Section IV analyzes the flow field mechanism. Finally, Sec. V summarizes the main findings.

II. NUMERICAL SIMULATION SETTING

A. Computational meshing and boundary conditions

In this study, a rigid model pressure measurement experiment of side-by-side square prisms is carried out in the wind tunnel laboratory of Chongqing University. The details regarding the experiment, along with the verification of the obtained results, are provided in Appendix. Meanwhile, to analyze the flow field mechanism further, a large eddy simulation is used to simulate the side-by-side square prisms. As shown in Fig. 1, ANSYS ICEM 2020 R2 software is used to complete the geometric modeling and flow field mesh division according to the wind tunnel dimensions. The static prism is the principal structure, and the vibrating prism, which is the interfering structure, can interfere with the principal one. They have the same length (D), width (D), and height (6.25D). The prism's distance from the computational domain inlet is 24.5D and 49.5D from the downstream outlet, with a lateral distance of 11.5D on each side. After the prisms are arranged in the computational domain, the maximum blockage ratio of the wind tunnel is 2.6%, which meets the requirement that the blockage ratio of the numerical simulation is less than 3%.[34,35] In this study, an O-block method is employed to refine the mesh within a 0.5D radius surrounding the structure. The minimum mesh thickness is set to 0.0006 m, with an exponential growth rate of 1.05. This approach ensures that the dimensionless wall distance (yPlus) remains below 1, ensuring high-precision resolution of the boundary layer. Additionally, the mesh in the structure is refined at both free end and bottom, with a minimum mesh size of 0.00328 m. The mesh growth in this region follows a biexponential pattern with a growth rate of 1.2, which enhances the numerical resolution at both the free and fixed ends of the structure. According to these grid division rules, the total number of grids in the computational domain amounted to 8×10^6.

For the setup of boundary conditions, the boundary condition at the inlet of the computational domain is set as a velocity inlet (velocity-inlet), and the outlet boundary condition is set as a fully developed free outflow (outflow). The prism and the left, right, top, and ground sides of the computational domain are set as no-slip walls (wall). For the side-by-side square prisms under FSI, the interfering structure with maximum vibration amplitude is $y_{max}/D = 10\%$, where y_{max}

28 November 2025 03:08:21

Published under an exclusive license by AIP Publishing

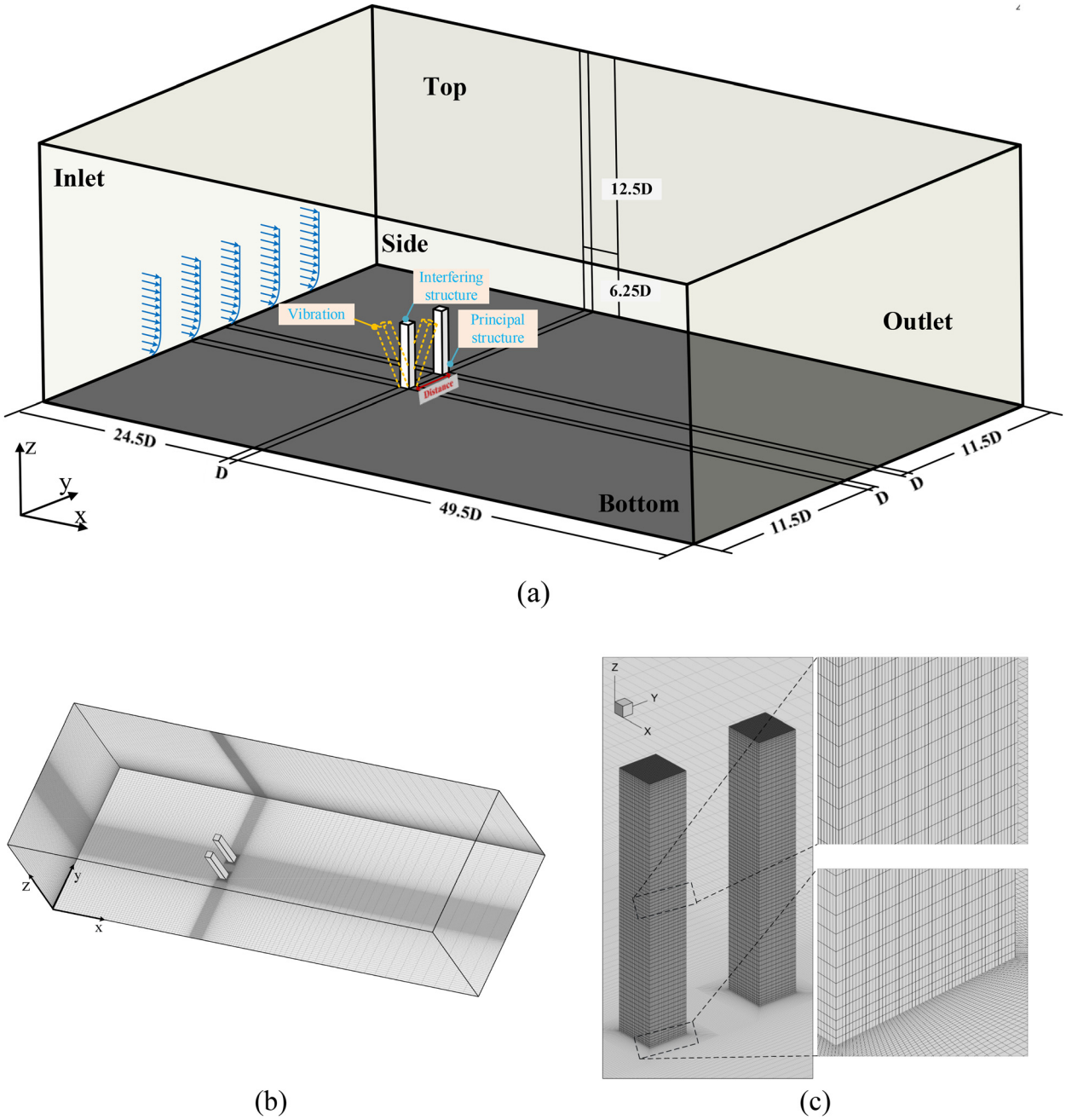

FIG. 1. Computational domain of side-by-side square prisms: (a) the computational domain, (b) the mesh of computational domain, and (c) the mesh of local domain.

represents the maximum displacement of the free end, and D is the characteristic size of the prism. Four representative cases are selected for analysis in this study, as shown in Table I.

B. Solution parameters and dynamic meshing setting

The settings for the large eddy simulation solution are detailed in Table II. This study employs the SIMPLEC algorithm for the solution method with the Smagorinsky–Lilly Model ($Cs = 0.1$). The pressure discretization is performed using a Second-Order scheme, while the time discretization adopts a Second-Order Implicit format. The gradient scheme is based on the Green-Gauss Node, and the momentum equations are discretized using the Bounded Central Differencing. The convergence criteria for the continuity equation and velocity components are a residual of 10^{-5}, with each computational iteration comprising 20 steps.

28 November 2025 03:08:21

Published under an exclusive license by AIP Publishing

TABLE I. Settings of four representative cases.

Conditions	Distance	Amplitude of interfering structure	Remark
Case 1	2D	$y_{max}/D = 0\%$	Rigid; small distance
Case 2	3D	$y_{max}/D = 0\%$	Rigid; large distance
Case 3	2D	$y_{max}/D = 10\%$	Forced vibration; small distance
Case 4	3D	$y_{max}/D = 10\%$	Forced vibration; large distance

TABLE II. The setting parameters of large eddy simulation.

Computational settings	Parameter settings
Solution method	SIMPLEC
Subgrid-scale model	Smagorinsky–Lilly Model
Pressure discretization	Second-Order
Time discretization	Second-Order Implicit
Gradient scheme	Green–Gauss Node Based
Momentum equations discretization	Bounded Central Differencing
Max iteration	20
Convergence criteria	10^{-5}

To ensure that the numerical solution of the Navier–Stokes equation does not diverge, the Courant–Friedrichs–Lewy (CFL) number is usually set to 1.

$$CFL = \frac{\Delta t \times U_{ref}}{\Delta x_{min}}, \tag{1}$$

where Δx_{min} is 0.0006 m, U_{ref} is 6 m/s, and the time step Δt is determined to be 1×10^{-4} s.

Moreover, the employment of a dynamic mesh in the study necessitates the consideration of an additional parameter, known as the "mesh Courant number." The mesh Courant number essentially measures the ratio of the physical distance that a particle travels during one time step to the spatial discretization size. It is a critical parameter in determining the stability of the numerical simulations. Typically, the mesh Courant number should be less than 1. This condition ensures that the information does not travel more than one mesh per time step.

$$C_{mesh} = \frac{u_{mesh}\,\Delta t}{\Delta x_{mesh}}, \tag{2}$$

where C_{mesh} represents mesh Courant number. u_{mesh} is the velocity at the mesh, and Δx_{mesh} is the characteristic length of the mesh (which can be the mesh width or diameter depending on the mesh). The "mesh Courant number" in this study remains below 1, which can ensure numerical convergence and the simulation results are both reliable and robust.

Figure 2(a) presents the schematic diagram of forced vibration numerical simulation. In this study, the motion mode of the interfering structure is set through the Fluent UDF. Considering only the first-order mode of the prism, in which the height is linearly related to the vibration amplitude, it can be treated as a rigid body motion. The vibration prism varies sinusoidally over time, with the maximum amplitude of 10% of the structural width and the frequency of 7.5 Hz. When configuring parameters for dynamic mesh, structural movement inevitably causes stretching, compression, and deformation of the mesh. The primary methods for mesh reconstruction based on dynamic mesh are Spring Smoothing, Layering, and Remeshing. Given the structural movement, this study employs the Spring Smoothing method to maintain mesh quality, with a spring constant factor set to 0.8, convergence precision set at 1×10^{-5}, and the number of iterations set to 50. As shown in Fig. 2(b), by placing a monitoring point at the top of the interfering structure, the time–displacement curve of its top is monitored. It can be found that the displacement curve satisfies the parameter setting of the forced vibration, demonstrating the effectiveness of the Fluent UDF.

C. Narrow band synthesis random flow generation

In order to simulate the B-category wind field of the Chinese standard in the wind tunnel, it is important to generate boundary

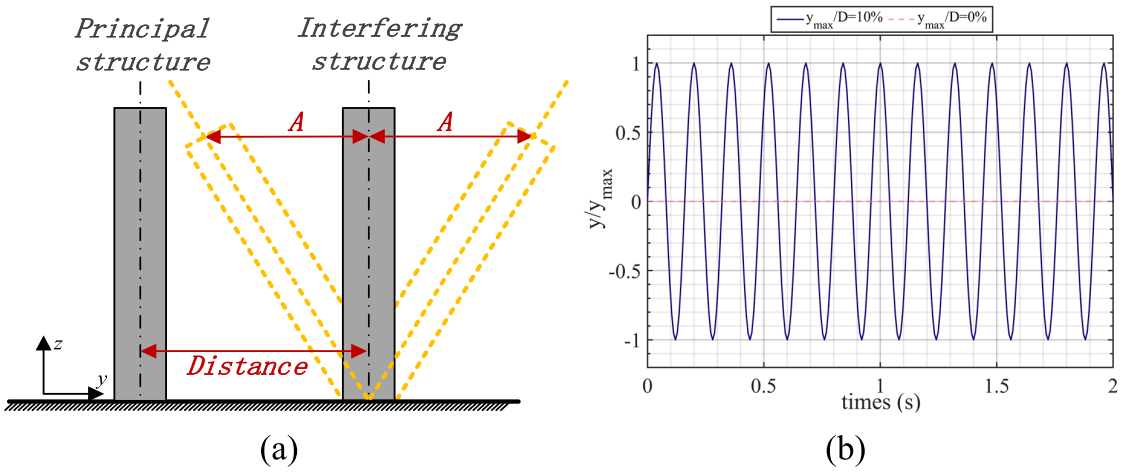

FIG. 2. Schematic illustration of the forced vibration: (a) diagram of the forced vibration And (b) the displacement curve at the top of the interfering structure.

28 November 2025 03:08:21

Published under an exclusive license by AIP Publishing

conditions with a realistic atmospheric boundary layer (ABL). This study utilizes the Narrow Band Synthesis Random Flow Generation (NSRFG)[36] method, which stringently ensures that the inlet turbulence meets continuity conditions. This method significantly enhances accuracy and efficiency compared to the previously used Random Flow Generation (RFG) series methods.[37,38] The NSRFG method[36] reconstructs the time series expression of the "harmonic unit," providing a theoretical foundation for the selection of parameters. The time domain superposition method is employed to reconstruct the single-point fluctuating velocity time series that meets the requirements. This is then expanded from a single point to a three-dimensional space, thereby constructing a fluctuating velocity field that satisfies the atmospheric boundary layer's zero divergence, spatial correlation, and fluctuating velocity power spectrum, among other turbulence characteristics. This approach leads to a more precise and efficient simulation of the large eddy simulation inlet turbulence velocity field, providing a solid foundation for the study of wind load assessment[39] and flow field phenomena[40] in high-rise buildings under ABL inflow conditions. Referring to the B-category wind field of the Chinese standard in the wind tunnel experiment, the basic parameters of NSRFG are shown in Table III.

III. VALIDATION AND AERODYNAMIC CHARACTERISTICS

A. Grid resolution validation

The large eddy simulation quality index (LES_IQ) is utilized to assess the applicability of grid resolution by evaluating the magnitude of the turbulent kinetic energy in the flow field.[41] If the grid resolution is too low, it may not accurately simulate the small-scale structures of the turbulent phenomenon, resulting in imprecise simulation results. When the grid resolution is high enough, LES_IQ approaches 1, indicating that the grid can effectively capture the details of turbulence, thereby yielding accurate simulation results. Based on the recommendations of Gousseau *et al.*[34] and Celik *et al.*,[41] LES_IQ range of 75%–85% is considered adequate for most engineering applications. These applications typically involve high Reynolds numbers, where the flow characteristics are complex and turbulent. The suggested range ensures a balance between computational efficiency and accuracy in capturing the essential flow dynamics. The calculation process of LES_IQ is as follows:

$$\mathrm{LES_IQ} = \frac{1}{1 + 0.05\left[\frac{\mu + \mu_{sgs}}{\mu}\right]^{0.53}}, \tag{3}$$

where μ_{sgs} is the sub-grid viscosity and μ is the fluid dynamic viscosity coefficient. Figure 3 shows the distribution of LES_IQ on the Z = 1/2H plane and the Y = ±1.5D plane. The results show that more than 80% of the resolution is achieved in the entire flow field, with the core area grid (around the prism and the near-wake region) even achieving a resolution of over 85%. However, the LES_IQ resolution is reduced in the prism and wake region. This is due to the local acceleration caused by the separation of the edge flow, and the velocity gradient suddenly increases and typically requires an extremely fine grid resolution to resolve. Overall, the LES_IQ resolution field is higher than 75% in the flow field, indicating that the core area grid has a high resolution for conducting subsequent research.

TABLE III. The flow parameters of the NSRFG method.

Parameters	Definition
Type of wind field	B-category wind field
Mean velocity	$U(z) = U_{\mathrm{ref}}\left(\frac{z}{z_{\mathrm{ref}}}\right)^{\alpha}$
	$U_{\mathrm{ref}} = 6\,\mathrm{m/s},\ Z_{\mathrm{ref}} = 0.6\,\mathrm{m},\ \alpha = 0.16$
Turbulence intensity	$I_u(z) = I_{\mathrm{ref}}\left(\frac{z}{z_{\mathrm{ref}}}\right)^{-\alpha}$
	$I_v(z) = I_u(z)\frac{\sigma_v}{\sigma_u}, I_w(z) = I_u(z)\frac{\sigma_w}{\sigma_u}$
Turbulent integral scale	$L_u(z) = 300\left(\frac{z}{300}\right)^{0.46+0.074\ln z_0}$
	$L_v(z) = 0.5\left(\frac{\sigma_v}{\sigma_u}\right)^3 L_u(z),$
	$L_w(z) = 0.5\left(\frac{\sigma_w}{\sigma_u}\right)^3 L_u(z)$

B. Wind field validation

The study employs the NSRFG method to generate the inlet turbulent wind field. Then, by setting a row of vertical monitoring points at the computational domain inlet (1D downstream from the inlet) and the structure location (1D ahead of the gap of the prisms), the velocity time series of each monitoring point can be collected, calculating the normalized wind profile U/U_r and turbulence intensity I_u. The comparison of the experimental and simulated wind characteristics is illustrated in Figs. 4–7. The simulation results of the wind field show that the mean velocity and turbulence intensity obtained by the simulation at the structure location and the inlet are almost consistent with the wind tunnel measurements, demonstrating the reliability of the large eddy simulation. However, the turbulence intensity and mean velocity at the structure location are slightly smaller than the target values at the inlet position. This is due to the filtering effect of large eddy simulation and the inherent characteristics of the NSRFG method,[42,43] i.e., the decay of high-frequency small-scale turbulence, resulting in the decay of turbulence intensity and wind profile from the inlet to the structure location.

Figure 8 compares the error analysis of wind field characteristics obtained from numerical simulations and experimental measurements. The calculation process for $Error_u$ and $Error_I$ is shown as follows:

$$Error_u = \frac{U_{LES} - U_{\mathrm{Exp}}}{U_{\mathrm{Exp}}} \times 100\%, \tag{4}$$

$$Error_I = \frac{I_{LES} - I_{\mathrm{Exp}}}{I_{\mathrm{Exp}}} \times 100\%. \tag{5}$$

Here, $Error_u$ represents the error in the wind profile, and Error_I represents the error in turbulence intensity. U_{LES} and I_{LES} denote the wind profile and turbulence intensity obtained from large eddy simulation, respectively. U_{Exp} and I_{Exp} denote the wind profile and turbulence intensity obtained from wind tunnel experiments, respectively.

From Fig. 8, it can be observed that the error values for both the wind profile and turbulence intensity are always less than 10%, whether at the inlet or at the structure. Additionally, the error in turbulence intensity is consistently greater than that in the wind profile. This

28 November 2025 03:08:21

Published under an exclusive license by AIP Publishing

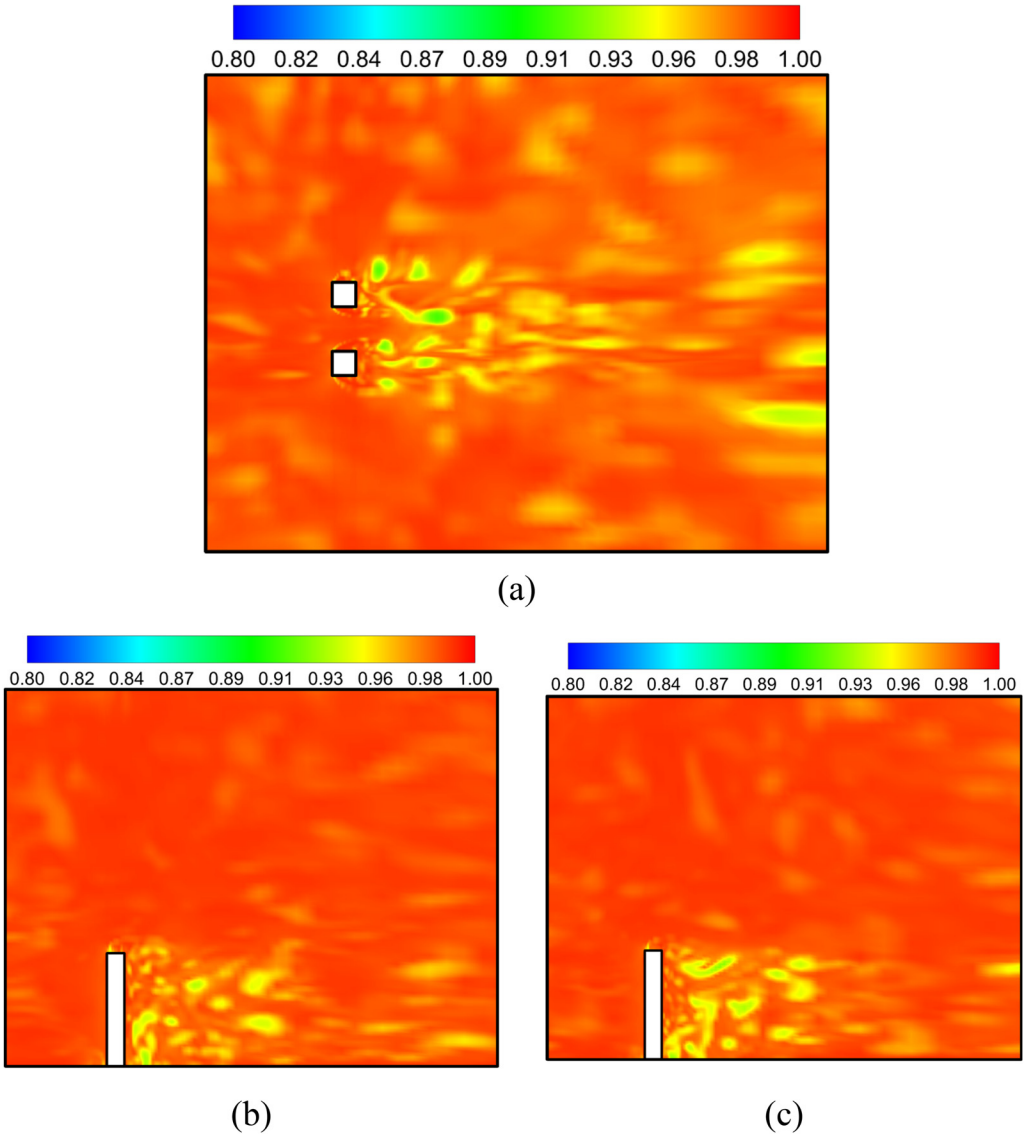

FIG. 3. LES_IQ of side-by-side square prisms: (a) LES_IQ of side-by-side square prisms at Z = 1/2H height (X–Y Plane); (b) longitudinal section of interfering structure (X–Z Plane, Y = 1.5D); and (c) longitudinal section of the principal structure (X–Z Plane, Y = −1.5D).

discrepancy may be attributed to the dissipation of high-frequency small-scale turbulence in the NSRFG method. Since the wind profile averages the time-history velocities, the impact of small-scale eddy dissipation on the wind profile is somewhat reduced.

C. Verification and analysis of aerodynamic characteristics

By performing a time-averaging process on the time-history pressure coefficients, the comparison of the mean pressure coefficients C_p at different heights from large eddy simulation and wind tunnel experiments for side-by-side square prisms with varying spacing is illustrated in Fig. 9. As illustrated in Fig. 26(c), this study compares levels 2, 4, 6, and 7 of the prisms. Observations indicate that the mean pressure coefficients of case 1 and case 2 obtained from large eddy simulation and wind tunnel experiments are consistent at different heights of the prism, indicating the effectiveness of the large eddy simulation results in this study. Points 1–4 and 9–12 represent the windward and leeward sides of the prism, while 5–8 and 13–16 are the right and left sides, respectively.

When the spacing between the side-by-side square prisms is 2D (i.e., case 1), as shown in Figs. 9(a) and 9(b), the mean pressure coefficients on the windward side of both the interfering structure and the principal structure increase with the height, peaking at level 6. Due to the end effect,[44] the mean pressure coefficient at the top of the prism decreases slightly. Meanwhile, the mean pressure coefficients on both

28 November 2025 03:08:21

Published under an exclusive license by AIP Publishing

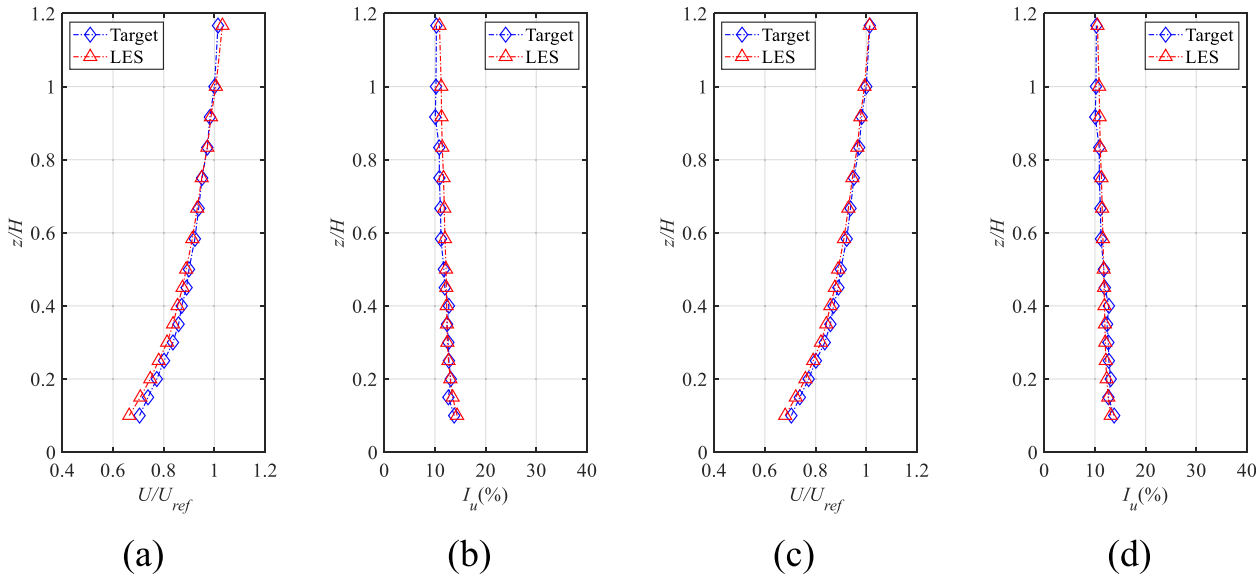

FIG. 4. Simulated and targeted wind characteristics for case 1: (a) inlet profile, (b) inlet profile, (c) structural profile, and (d) structural turbulence intensity.

sides of the interfering and principal structures are negative due to the flow separation over the windward side, creating a negative pressure region in the crosswind direction. Notably, there is a significant change in the mean pressure coefficients on the left side of the interfering structure (points 13–16) and the right side of the principal structure (points 5–8). This change is attributed to the narrow pipe effect, which causes the flow at the gap between the two prisms to accelerate. According to Bernoulli's principle, an increase in dynamic pressure leads to a decrease in static pressure, hence the reduction in pressure coefficients in the gap. In addition, an asymmetry in the mean pressure coefficients on the left and right sides of the interfering and principal structure is observed.

When the spacing between the side-by-side square prisms is 3D (i.e., case 2), as shown in Fig. 9(c) and 9(d), with the increase in the spacing, the mean pressure coefficient on the windward side does not change significantly and shows a trend of increasing with the height. The flow separation also causes negative pressure regions on both sides of the prism and the leeward side. However, it is worth noting that with the increased spacing, the negative mean pressure coefficient on both sides of the gap decreases, which indicates the weakening of the

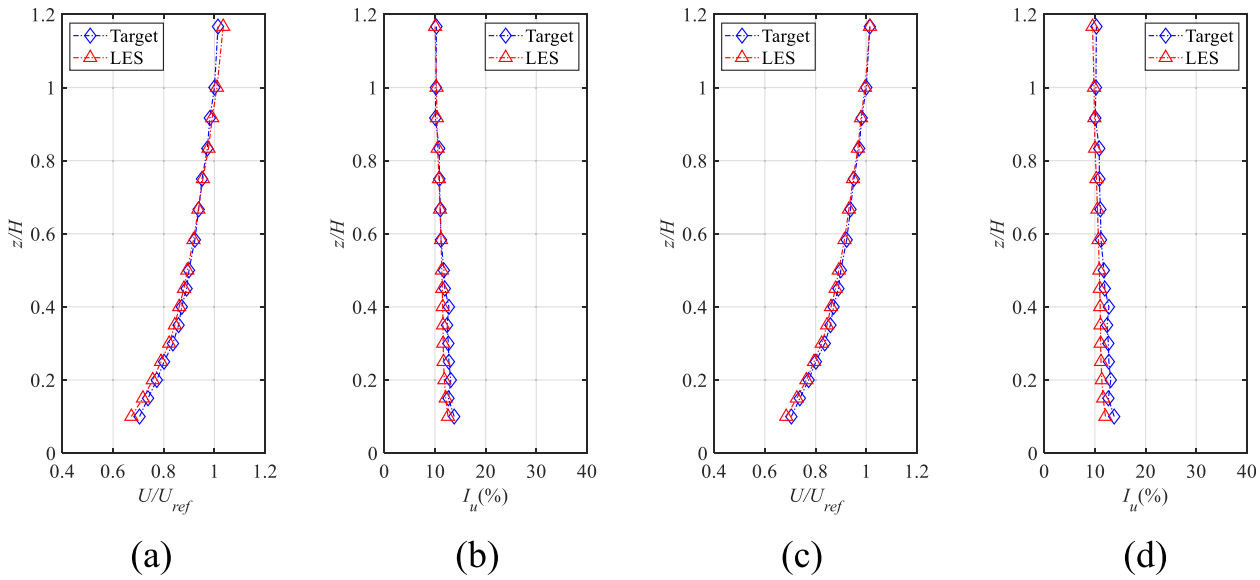

FIG. 5. Simulated and targeted wind characteristics for case 2: (a) inlet profile, (b) inlet profile, (c) structural profile, and (d) structural turbulence intensity.

28 November 2025 03:08:21

Published under an exclusive license by AIP Publishing

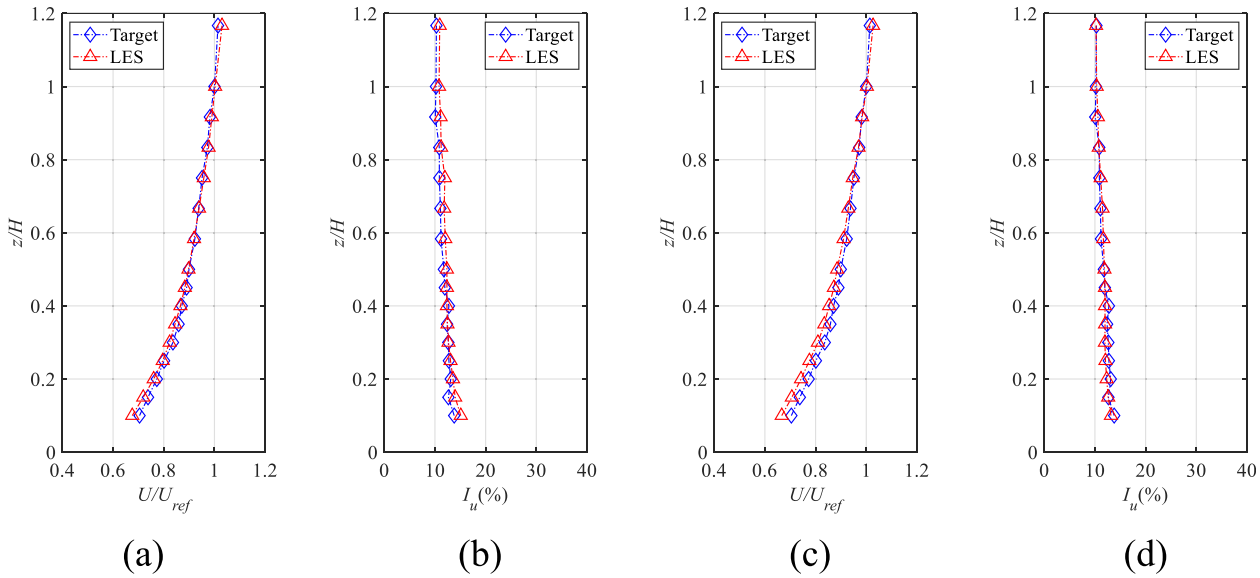

FIG. 6. Simulated and targeted wind characteristics for case 3: (a) inlet profile, (b) inlet profile, (c) structural profile, and (d) structural turbulence intensity.

interference effect. For the interfering structure, the negative mean pressure coefficient on the left side (measurement points 13–16) is greater than the mean pressure coefficient on the right side (measurement points 5–8).

Figure 10 compares the mean pressure coefficients of the side-by-side square prisms with different spacing, taking into account the FSI. For the side-by-side square prisms with a spacing of 2D (i.e., case 3), it can be observed from Fig. 10(a) that the mean wind pressure coefficient on the windward side of the interfering structure increases continuously along the height direction, with notable end effect at the top. Due to the flow separation occurring on the windward side, the mean pressure coefficients on both sides and the leeward side of the interfering structure are negative. Similarly, as shown in Fig. 10(b), for the principal structure, its windward side, leeward side, and sides all show a similar trend to the interfering structure. With the increase in the spacing to 3D (i.e., case 4), as shown in Fig. 10(c), compared to the 2D spacing, the mean pressure coefficients on the windward side, leeward side, and right side of the interfering structure do not change significantly. Similarly, as shown in Fig. 10(d), the change in the principal structure's mean pressure coefficient is consistent with the interfering

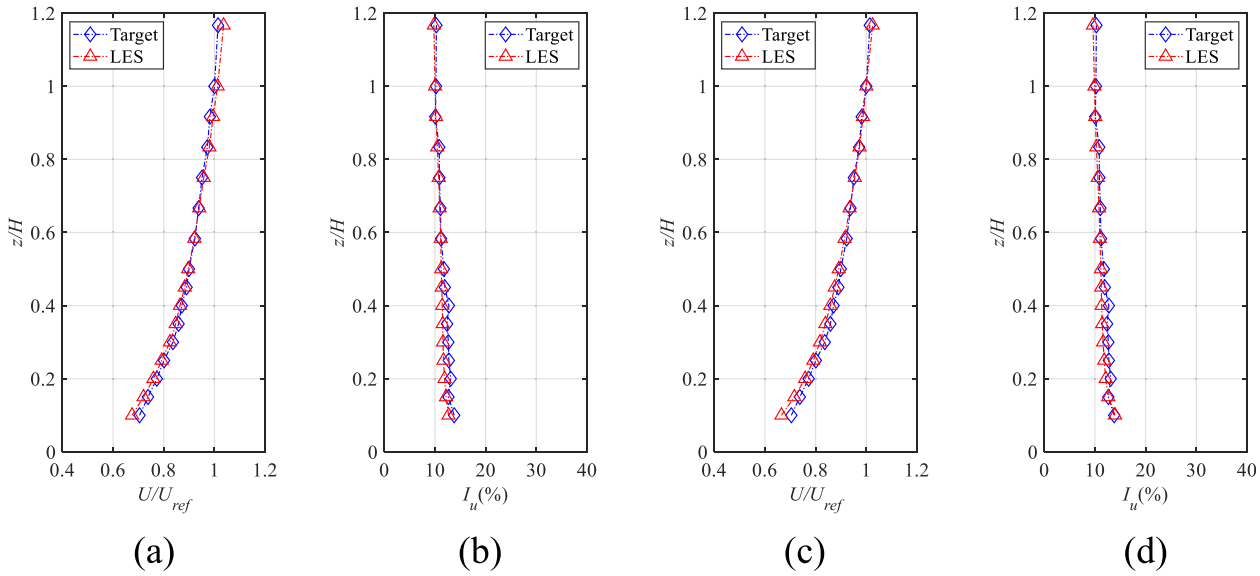

FIG. 7. Simulated and targeted wind characteristic for case 4: (a) inlet profile, (b) inlet profile, (c) structural profile, and (d) structural turbulence intensity.

28 November 2025 03:08:21

Published under an exclusive license by AIP Publishing

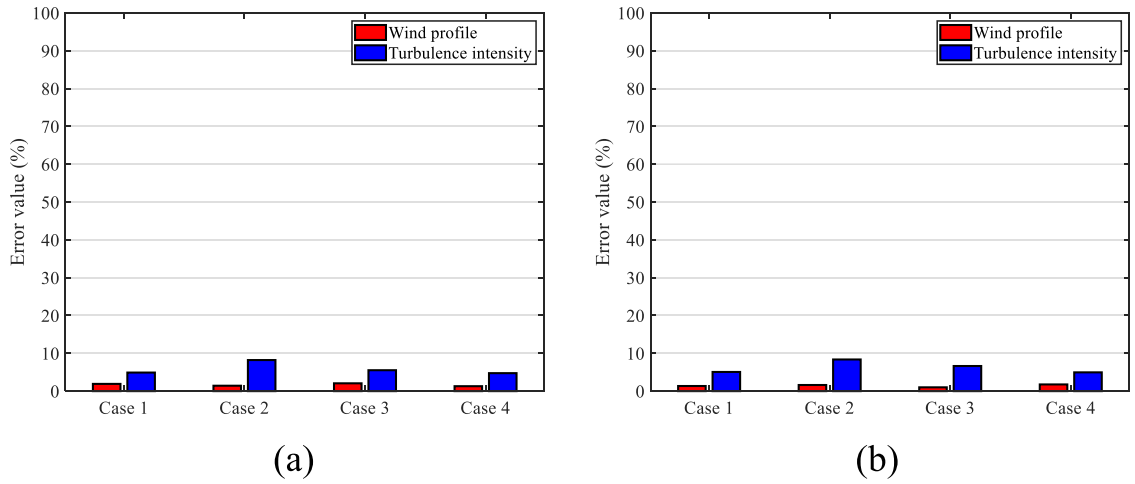

FIG. 8. Error analysis of wind characteristics: (a) calculated error value at the inlet and (b) calculated error value at the structure.

structure. Additionally, it is also observed that the negative pressure on both sides of the gap between the prisms abruptly decreases due to the weakened interference effect with the increased spacing.

In addition to the influence of spacing on mean pressure coefficients, the vibration of the interfering structure also has an impact. Compared to the stationary side-by-side 2D prism with the forced vibration side-by-side 2D prism [Figs. 10(a) and 10(b)], the vibration of the interfering structure has little effect on the mean pressure coefficient on its windward side. However, the negative pressure on the leeward side increases, especially at the top. This is because the prism vibrates periodically with an amplitude that increases with the height of the prism. Thus, the top of the prism is most affected. Additionally, the negative pressure on the right side of the interfering structure under vibration increases slightly, while the negative pressure on the left side increases significantly. For the principal structure, the windward and leeward sides remain largely unchanged, while the two sides show an increasing trend.

As the spacing increases, the influence of structural vibration gradually weakens. Specifically, by comparing the stationary side-by-side square prisms with the forced vibration side-by-side square prisms [Figs. 10(c) and 10(d)], for the interfering structure, the interference effect between the two prisms gradually weakens under the 3D spacing, but the influence of vibration still exists. To be specific, the negative mean pressure coefficient by the left and right sides of the interfering structure is noticeable greater than that of the stationary structure. However, for the principal structure, there is a slightly increase in the negative pressure on its left and right side, while the mean pressure coefficients on the leeward sides do not change significantly.

IV. FLOW FIELD MECHANISM

In this study, the mechanism of the side-by-side finite-length square prisms under rigid and vibration is investigated. By employing the large eddy simulation, the flow field morphology of the side-by-side square prisms at different spacing under FSI is revealed. Initially, three specific positions at different heights of the side-by-side square prisms are selected—Z = 1/6H, Z = 1/2H, and Z = 5/6H—and two cross sections along the Y-direction. The specific flow field cross section is shown in Fig. 11.

A. Time-averaged streamline characteristics

The aerodynamic characteristics and time-averaged streamlines of the side-by-side square prisms are both responses to the time-averaged characteristics of the structure and have a strong correlation. By analyzing time-averaged streamlines, this study established a connection between aerodynamic characteristics and flow field phenomena, laying a foundation for further understanding the flow mechanism in side-by-side square prisms.

Figure 12 shows the time-averaged streamlines and mean velocity of the side-by-side square prisms at different heights. It can be observed from the figure below that the time-averaged streamlines of the side-by-side square prisms are symmetrically distributed. When the flow reaches the interfering and principal structure, flow separation occurs on both sides, resulting in small-scale leading-edge vortices on both sides and large-scale trailing-edge vortices on the back. However, the velocity in the gap between the interfering structure and the principal structure increases significantly. It can be observed from Fig. 12 that the streamlines converge in the gap, and the spacing between the streamlines decreases, indicating an acceleration of the flow, which is called the narrow pipe effect.

When the spacing between the side-by-side square prisms is 2D, the flow morphology is expected to be in the two-frequency regime, as mentioned by Alam *et al.*[20] However, it can be observed from Figs. 12(a), 12(c), and 12(e) that there is no biased gap flow between the two prisms, and the flow morphology tends to be the transition regime. This is because, for finite-length side-by-side square prisms, the inflow and the flow at the top of the prism are replenished into the gap, providing sufficient streamwise momentum to prevent deviation. Additionally, due to the small spacing between the interfering structure and the principal structure, the gap flow acceleration is more significant, which in turn causes the leading-edge vortex to be squeezed and disappear. Moreover, the time-averaged streamlines in the gap converge, and the spacing between the streamlines decreases. The narrow

28 November 2025 03:08:21

Published under an exclusive license by AIP Publishing

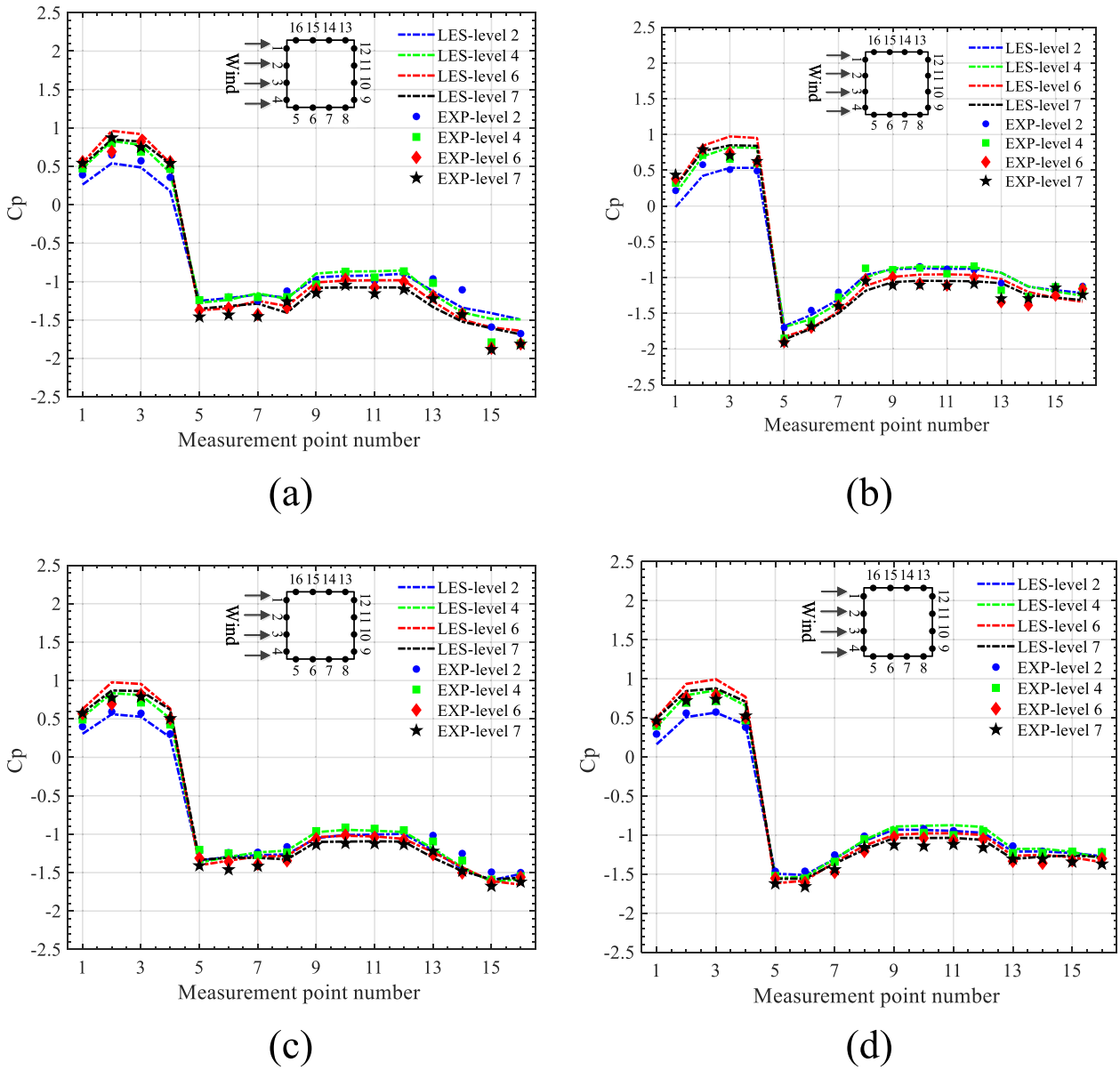

FIG. 9. Comparison of mean pressure coefficients for case 1 (stationary) and case 2 (stationary): (a) interfering structure in case 1, (b) principal structure in case 1, (c) interfering structure in case 2, and (d) principal structure in case 2.

gap forms a spatial constraint for the lateral expansion of the trailing vortex, causing the trailing vortex to be "squeezed" and thus become thinner, transforming the originally symmetric bi-vortex structure into a slender vortex structure.

When the spacing between the side-by-side square prisms is 3D, it can be observed from Figs. 12(b), 12(d), and 12(f) that the flow morphology, which should be in the transition regime, also tends to be the coupled vortex street (CVS) regime due to the replenishment of flow at the top of the prisms. As the spacing increases, the flow acceleration slows down relatively, no longer creating a sufficient pressure gradient to inhibit the formation of a leading-edge vortex. The leading-edge vortex, which had previously disappeared between the interfering and principal structure, reappears. At the same time, the larger spacing allows for better spatial development of the wake vortex. The constraining effect of vortex squeezing diminishes with increased spacing, making the previously slender vortex structures in the gap more symmetric. In summary, due to the replenishment of flow at the top of the finite-length side-by-side square prisms, the gap flow has enough streamwise momentum to prevent deflection. At the same time, the "squeezing" of the gap flow leads to the convergence of time-averaged

28 November 2025 03:08:21

Published under an exclusive license by AIP Publishing

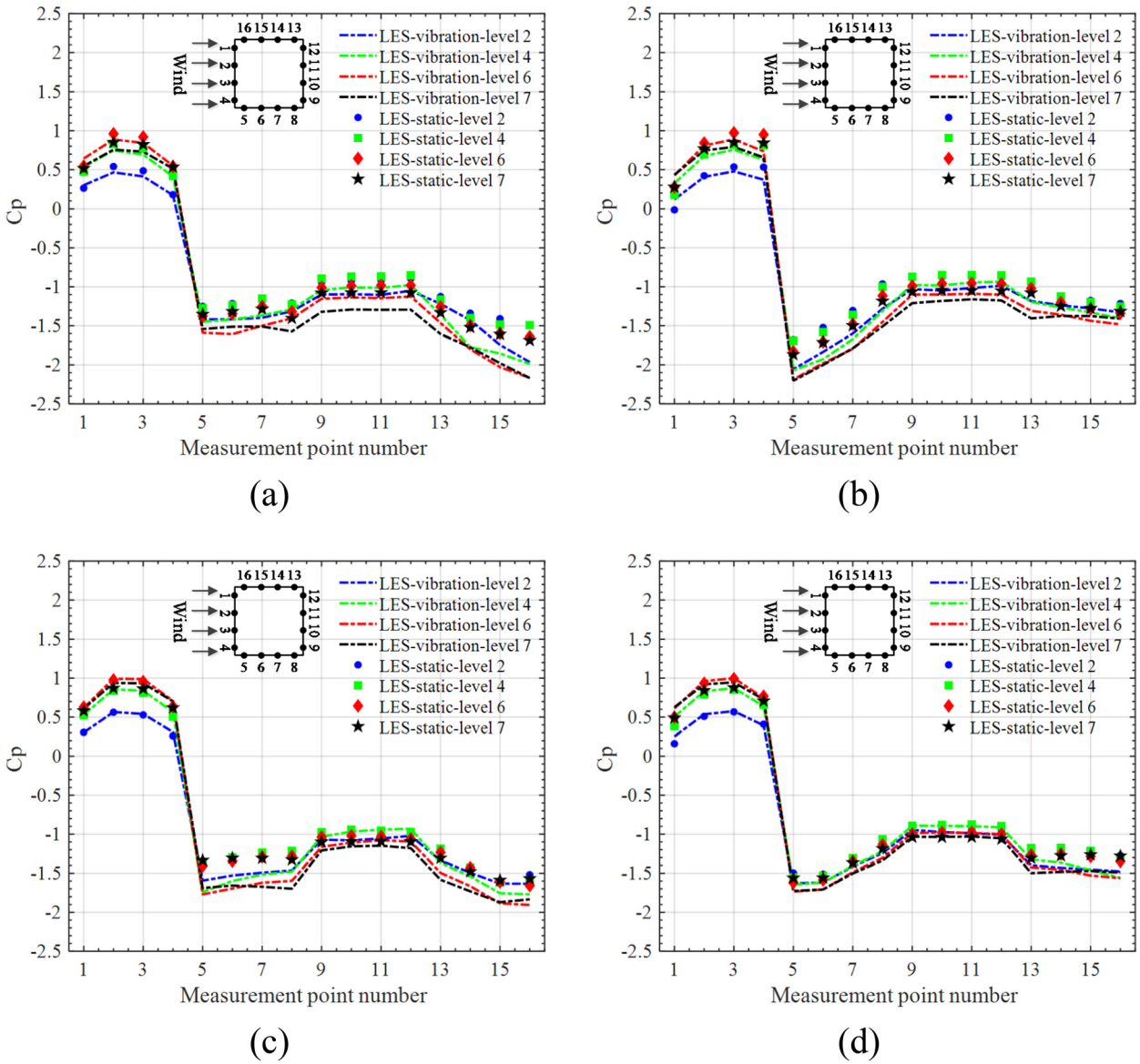

FIG. 10. Comparison of mean pressure coefficients for case 3 (vibration) and case 4 (vibration): (a) interfering structure in case 3, (b) principal structure in case 3, (c) interfering structure in case 4, and (d) principal structure in case 4.

streamlines, internal compression, elongation at the rear, and changes in the position and extent of the wake vortex. These changes directly affect the pressure distribution on the surface of the structure, significantly impacting lift and drag.

Figure 13 illustrates the time-averaged streamlines and mean velocity of the side-by-side square prisms at different heights under FSI, showing distinct regimes for different spacing. When the spacing between the side-by-side square prisms is 2D, as shown in Figs. 13(a), 13(c), and 13(e), the structural vibration causes the gap flow to deflect toward the side of the vibration, so that the gap flow divides the wake into a narrow streets and a wide streets region, the flow morphology should be the two-frequency regime. This is because the structural vibration increases the curvature of the shear layer of the interfering structure, and then the vortex separated from the trailing edge of the structure has enough lateral momentum to induce the gap flow toward the side of the structural vibration. As pointed out by existing studies,[20–22,24] the structural vibration causes the gap flow to deflect, resulting in a narrower street width of the interfering structure, a shorter recirculation region length, an increased wake velocity, and thereby increasing the negative pressure on the leeward side of the interfering structure. Additionally, as the gap flow deflects to the interfering structure, the negative pressure on the side of the interfering structure near the gap also increases.

28 November 2025 03:08:21

Published under an exclusive license by AIP Publishing

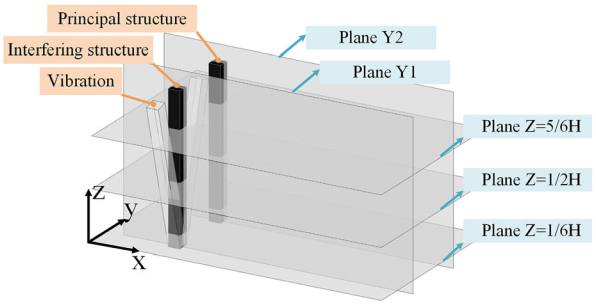

FIG. 11. Schematic of flow field section of side-by-side square prisms.

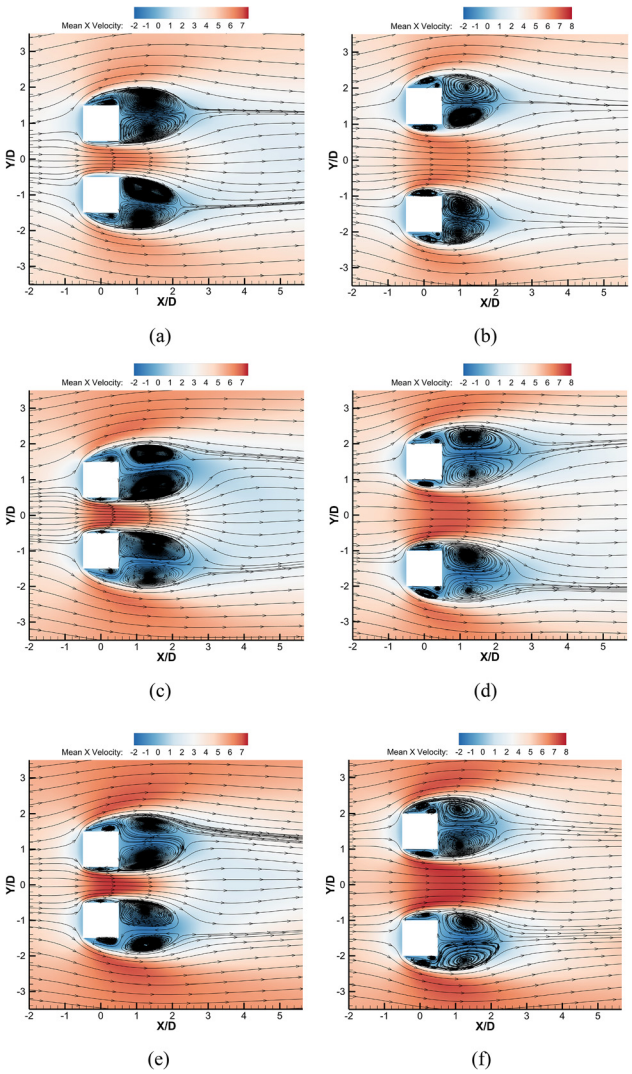

FIG. 12. Time-averaged streamlines and mean velocity at different heights of side-by-side square prisms (m/s): (a) Z = 1/6H plane in case 1, (b) Z = 1/6H plane in case 2, (c) Z = 1/2H plane in case 1, (d) Z = 1/2H plane in case 2, (e) Z = 5/6H plane in case 1, and (f) Z = 5/6H plane in case 2.

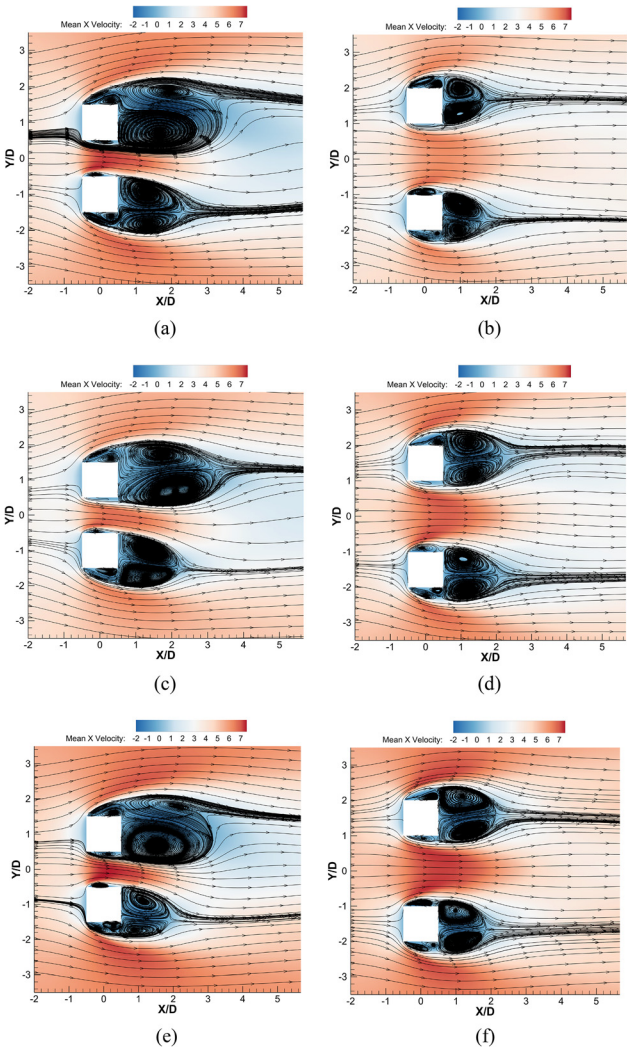

FIG. 13. Time-averaged streamlines and mean velocity at different heights when side-by-side square prisms vibrate (m/s): (a) Z = 1/6H plane in case 3, (b) Z = 1/6H plane in case 4, (c) Z = 1/2H plane in case 3, (d) Z = 1/2H plane in case 4, (e) Z = 5/6H plane in case 3, and (f) Z = 5/6H plane in case 4.

When the spacing between the side-by-side square prisms continues to increase to 3D [as shown in Figs. 13(b), 13(d), and 13(f)], the flow field remains symmetrically distributed due to the sufficient gap between the prisms. Here, the gap flow, having enough streamwise momentum from the inflow, is not sufficiently induced by the prism's vibration to deflect. However, the structural vibration increases the lateral momentum of the gap flow, intensifying the compression of the wake region between the two prisms. This compression shortens the recirculation region and squeezes the leading edge vortices at the sides of the gap, thinning or even disappearing, leading to an increase in negative pressure on the inner sides of both structures. In summary, the lateral vibration of the prism increases the lateral momentum of the fluid around the prism. For 2D spacing, the gap flow with less streamwise momentum is induced to deflect toward the side of the

28 November 2025 03:08:21

Published under an exclusive license by AIP Publishing

vibration. For 3D spacing, the gap flow compresses the length of the recirculation region and reduces the thickness of the leading edge vortices on the inner sides of the structures.

Figure 14 shows the recirculation and mean velocity of the longitudinal section of the side-by-side square prisms with different spacing. The figure reveals that when the inflow reaches the windward side, a stagnation point forms at 2/3 of the interfering and principal structure. Above the stagnation point, the flow moves upward along the structure, crossing over its top. Due to the separation of the shear layer, a small-scale vortex forms at the top and a large-scale vortex forms at the back. Simultaneously, the large-scale vortex on the leeward side creates a significant negative pressure at this location. The flow at the upper part of the free end is drawn downward, forming a downwash flow. Likewise, the flow at the base is drawn upwards, creating an upwash flow.

For the spacing between side-by-side square prisms being 2D, it can be observed from Figs. 14(a) and 14(b) that the space between the two prisms is limited, which leads to the enhancement of the vortex interaction between them. Such interaction promotes the reattachment of inflow at the backside of the free end, more readily forming

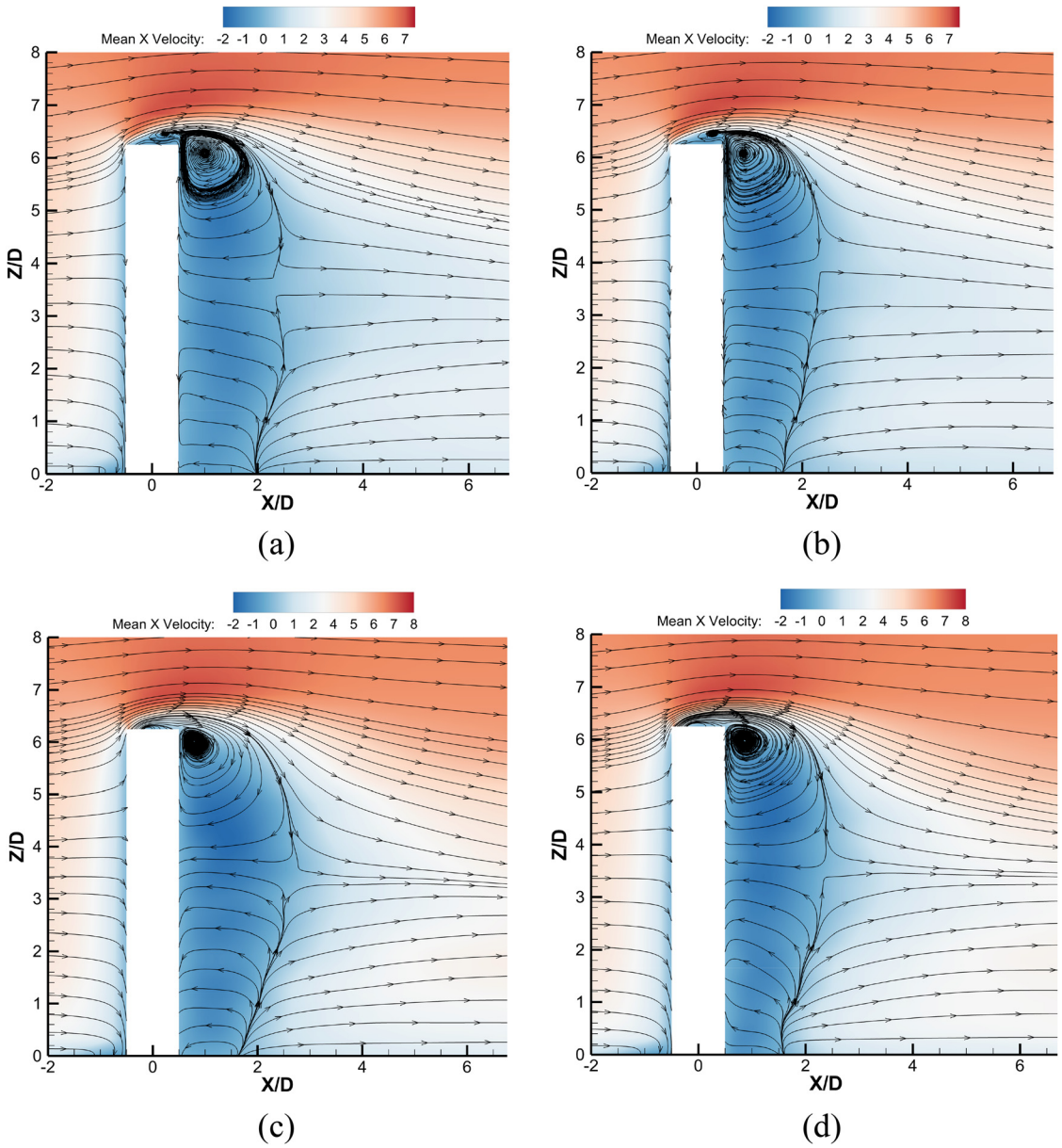

FIG. 14. Time-averaged streamlines and mean velocity of the longitudinal section of the side-by-side square prisms (m/s): (a) Y1 = −1D plane in case 1, (b) Y2 = 1D plane in case 1, (c) Y1 = −1.5D plane in case 2, and (d) Y2 = 1.5D plane in case 2.

28 November 2025 03:08:21

Published under an exclusive license by AIP Publishing

larger-scale vortices compared to a spacing of 3D. Moreover, a smaller spacing means that the fluid flowing between the two prisms will generate more turbulence. Turbulence, a flow with a rotational characteristic, transfers kinetic energy to the vortex, thereby enhancing the strength and size of the vortex at the free end of the side-by-side square prisms.

For the spacing between side-by-side square prisms being 3D, as observed from Figs. 14(c) and 14(d), as the spacing between side-by-side square prisms increases, the velocity in the gap decreases. The development and maintenance of the vortex is not interfered with by the adjacent structure, which makes the vortex formed on the back of the structure more independent. Compared to a spacing of 2D, the strength and size of the vortex at the free end are smaller. Under the larger spacing, the vortex from the back of the interfering structure and the principal structure cannot exchange momentum, resulting in weaker interactions between them at the free end, thereby decreasing the size of the vortices formed at the back.

When the prism vibrates, the time-averaged streamlines of the longitudinal section of side-by-side square prisms with a spacing of 2D are shown in Figs. 15(a) and 15(b). Due to vibration, the wide and narrow streets in the longitudinal section can also be clearly observed. The

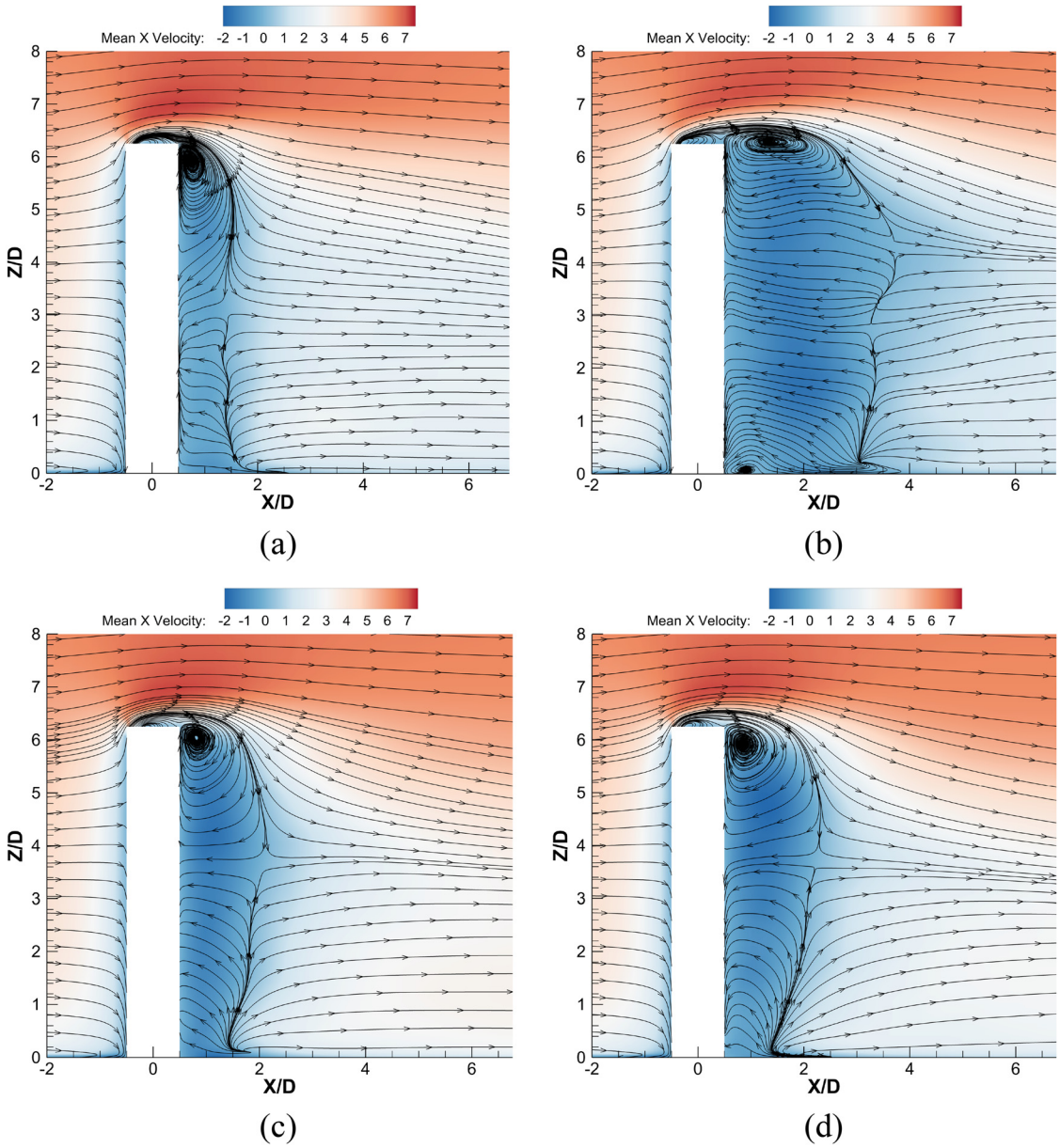

FIG. 15. Time-averaged streamlines and mean velocity of the longitudinal section when side-by-side square prisms vibrate (m/s): (a) Y1 = −1D plane in case 3, (b) Y2 = 1D plane in case 3, (c) Y1 = −1.5D plane in case 4, and (d) Y2 = 1.5D plane in case 4.

28 November 2025 03:08:21

Published under an exclusive license by AIP Publishing

size of the recirculation region around the interfering structure is significantly smaller than that of the principal structure's recirculation region. This might be because the downwash in the wake of the interfering structure plays a more significant role. In other words, the vibration enhances the downwash intensity in the wake of the interfering structure. Additionally, it can be observed that as the principal structure's recirculation region increases, the saddle point in the recirculation region (the point where no streamline passes, known as the saddle point) increases from one to two.

As the spacing increases to 3D, as shown in Figs. 15(c) and 15(d), the vibration can no longer divide the wake into wide and narrow streets, and the influence of the vibration is weakened. However, compared with the recirculation region of the stationary interfering structure [Fig. 14(c)], it can be seen that the size of the recirculation region around the interfering structure is significantly smaller when vibrating. This is likely because the vibration enhances the downwash in the wake of the interfering structure, thereby reducing the size of its recirculation region. However, due to the larger spacing between the two prisms, the vortices in the wake are less affected by the adjacent prism, preventing the principal structure from developing into a wide street.

The mean pressure coefficient contours of the windward side of prisms for the four cases are shown in Fig. 16. The figure reveals that contours of both the interfering structure and the principal structure are roughly symmetrical. The maximum mean pressure coefficient of 0.9 occurs around 0.7H (level 6), corresponding to the stagnation region where the flow splits into upwash and downwash. Above and below this height, the pressure slightly decreases due to flow separation. Moreover, the inner sides of the prisms [the right side of Fig. 16(a) and the left side of Fig. 16(b)] are affected by high-speed shear flow, resulting in a narrow pipe effect. The contours tend to shift toward the outer sides [the left side of Fig. 16(a) and the right side of Fig. 16(b)]. Additionally, when the spacing between the two prisms is 2D (cases 1 and 3), vibration causes a slight decrease in the pressure coefficients on the windward side of the prisms. However, when the spacing increases to 3D (cases 2 and 4), vibration has little effect on the contour.

B. Time-averaged vortex structure in the wake

In this study, the time-averaged vortex structure of the wake flow field is identified using the Q criterion[45,46] value of 26 and is colored by the mean × velocity. The time-averaged vortex structure of the side-by-side square prisms under different spacing is shown in Fig. 17. It can be observed from the figure that when the fluid flows through the windward side, flow separation occurs, and two adjacent counter-rotating dipole vortices are generated at the tail of each prism. Simultaneously, these dipole vortices expand and extend downward along the leeward direction, a process related to the downwash flow

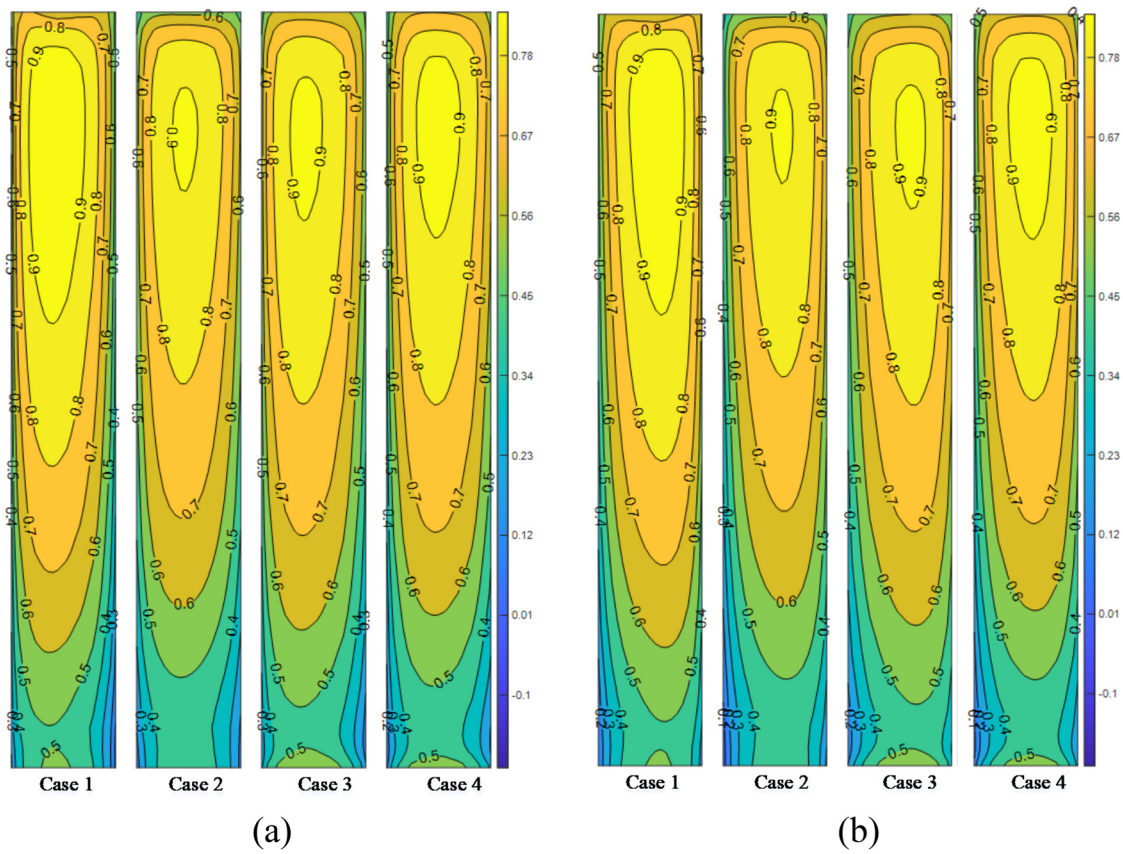

FIG. 16. Mean pressure coefficient contours of the windward side of prisms: (a) principal structure and (b) interfering structure.

28 November 2025 03:08:21

Published under an exclusive license by AIP Publishing

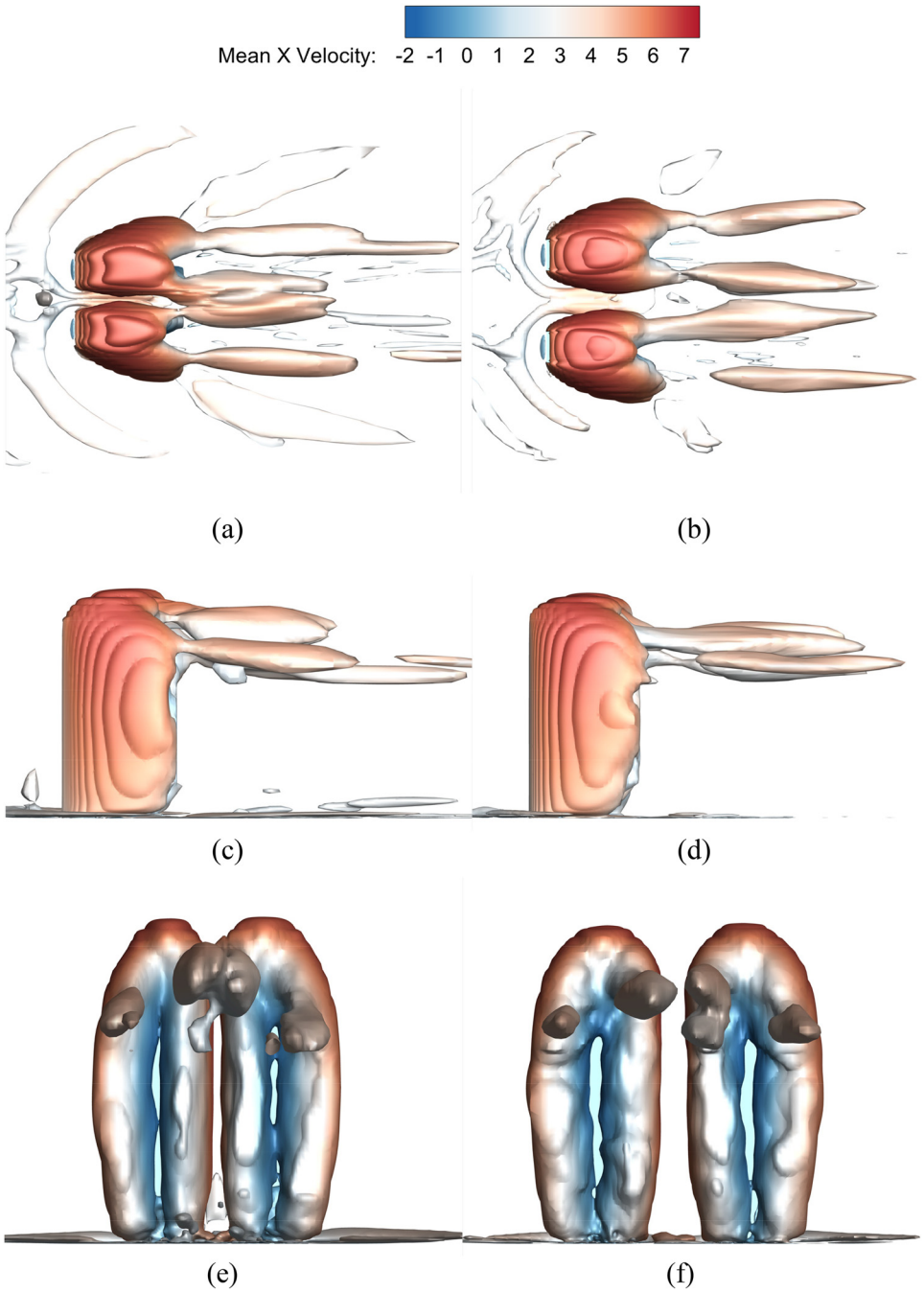

FIG. 17. Comparison of time-averaged vortex structures of side-by-side square prisms: (a) a top view of case 1, (b) a top view of case 2, (c) a lateral view of case 1, (d) a lateral view of case 2, (e) a side view of case 1, and (f) a side view of case 2.

from the prisms. The downwash flow also affects the generation and development of the dipole vortex, thereby altering the characteristics of the entire flow field.

For the spacing of 2D, as seen in Figs. 17(a), 17(c), and 17(e), when the adjacent dipole vortices are closer, their interaction is more significant, resulting in their merging. The size of the newly merged vortex depends on the size of the two original vortices and the interaction pattern. This merged phenomenon further strengthens the development of the vortex structure and makes the vortex structure in it more complex and chaotic. For the spacing of 3D, it can be observed from Figs. 17(b), 17(d), and 17(f) that the merged dipole vortices separate into more independent vortex structures. These independent dipole vortices exist relatively stable in space, maintaining their individual motion characteristics. The separated vortices no longer merge, forming a relatively stable flow pattern.

28 November 2025 03:08:21

Published under an exclusive license by AIP Publishing

As shown in Figs. 18(a), 18(c), and 18(e), when the structure vibrates at a small spacing, the dipole vortices at the free end of the principal structure migrates toward the interfering structure, resulting in a shortened dipole vortex length and increased lateral width. Furthermore, the compression of the space at the trailing edge of the interfering structure disrupts the formation of a complete dipole vortices. When the spacing increases to 3D, as illustrated in Figs. 18(b), 18(d), and 18(f), the vibration causes originally independent vortex structures to merge again. The length of the inner merged vortex structure is significantly shorter than that of the outer unmerged vortex structure. This merging phenomenon facilitates the development of the vortex structure, destabilizing the previously stable flow pattern.

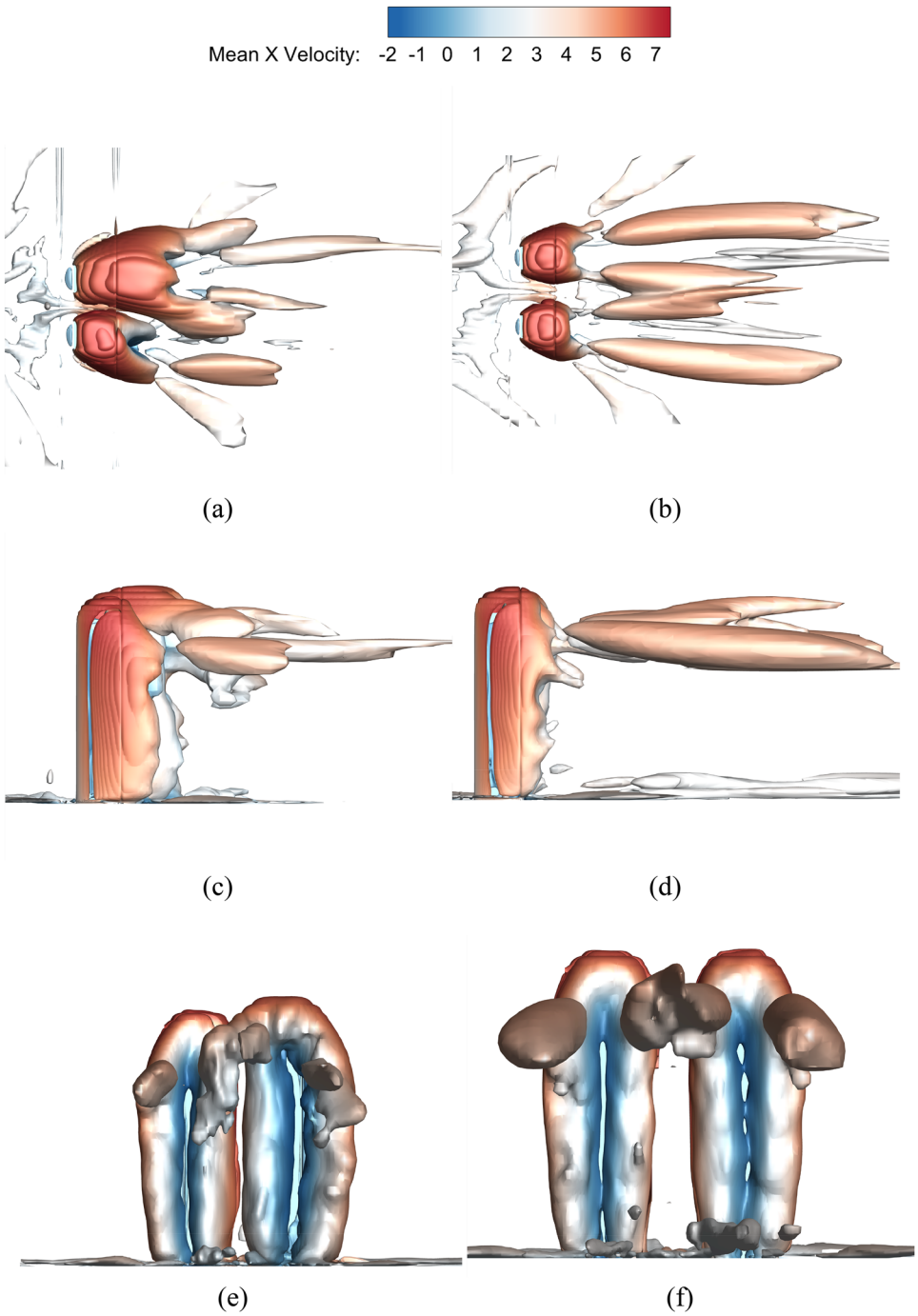

FIG. 18. Comparison of time-averaged vortex structures when side-by-side square prisms vibrate: (a) a top view of case 3, (b) a top view of case 4, (c) a lateral view of case 3, (d) a lateral view of case 4, (e) a side view of case 3, and (f) a side view of case 4.

28 November 2025 03:08:21

Published under an exclusive license by AIP Publishing

C. Spanwise instantaneous vorticity

In this study, considering that the prism is under periodic forced vibration, it is essential to carry out an instantaneous analysis of the flow field phenomenon. The flow field phenomenon at key positions is collected at a time interval of 1.25 T, as shown in Fig. 19. The sampling duration is at least four vortex shedding cycles, where t_i represents the sampling time point, and T represents the vibration period of the prism.

Figure 20 displays the instantaneous spanwise vorticity of the side-by-side square prisms with a spacing of 2D under both stationary and forced vibration. A slice is selected at the mid-span height of the prisms, Z = 1/2H, where t_1–t_4 is the instantaneous spanwise vorticity at different moments. Overall, the flow impacts the windward side of the two prisms, causing flow separation at the leading edge and resulting in alternating shedding vortices. However, due to the interaction of the wake between the two prisms, the flow field becomes complex and unstable. Specifically, as observed from Figs. 20(a), 20(c), 20(e), and 20(g), when the flow impacts the interfering structure and the principal structure, it creates shear layer separation, leading to alternating shedding vortices generated at the trailing edges of the structures. The proximity of the interfering structure and the principal structure causes the merging of wake-shedding vortices, accompanied by a narrow pipe effect between the prisms, narrowing the shear layer between them. This phenomenon reveals the impact of interaction between side-by-side square prisms on the flow field. Additionally, the gap flow between prisms tends to randomly favor one side or remain undeflected, indicating a transition regime.

Observations from Figs. 20(b), 20(d), 20(f), and 20(h) reveal that when the prism vibrates, the curvature of the shear layer between the two prisms increases and the momentum thickness decreases, resulting in an accelerated vortex shedding frequency. Consequently, this leads to a greater intensity of the vortices in the wake region of the interfering structure. A pair of cross-stream vortices in the interfering structure wake usually form a coupling, creating a low-pressure region situated between the vortices and attract a gap vortex residing in the principal structure wake. Under the combined effect of these three vortex flows, the gap flow is deflected toward the side of the vibrating prism, consistent with findings by Liu and Jaiman.[25] Additionally, the vibration of the interfering structure increases the turbulence intensity, causing the wake vortices to become more fragmented.

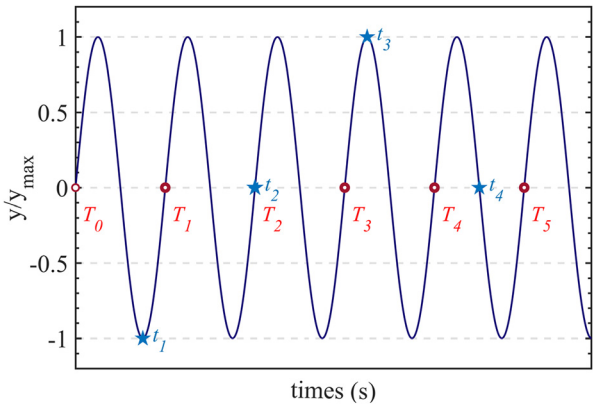

FIG. 19. Sampling time of flow field data considering FSI.

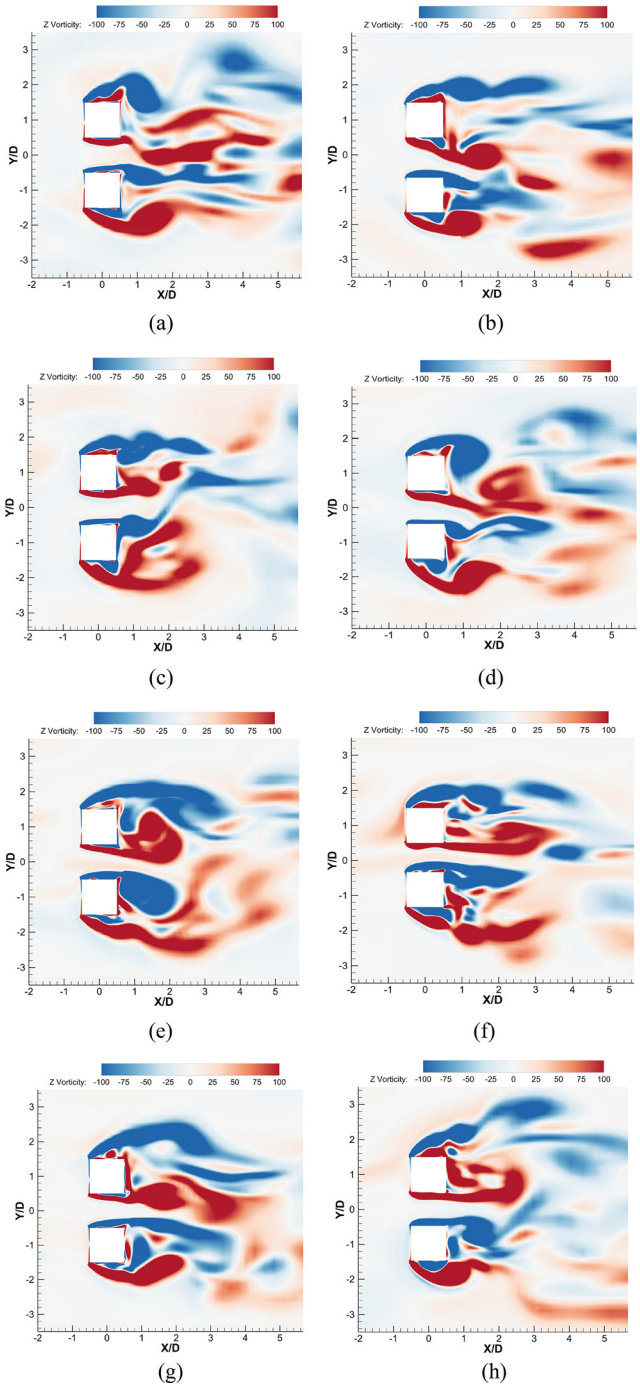

FIG. 20. Comparison of spanwise instantaneous vorticity between case 1 (stationary) and case 3 (vibration): (a) case 1 t_1, (b) case 3 t_1, (c) case 1 t_2, (d) case 3 t_2, (e) case 1 t_3, (f) case 3 t_3, (g) case 1 t_4, and (h) case 3 t_4.

As shown in Fig. 21, this study analyzes the instantaneous spanwise vorticity of the side-by-side square prisms with a 3D spacing under both stationary and forced vibration. For the stationary case at a 3D spacing, it can be observed from Figs. 21(a), 21(c), 21(e), and 21(g)

28 November 2025 03:08:21

Published under an exclusive license by AIP Publishing

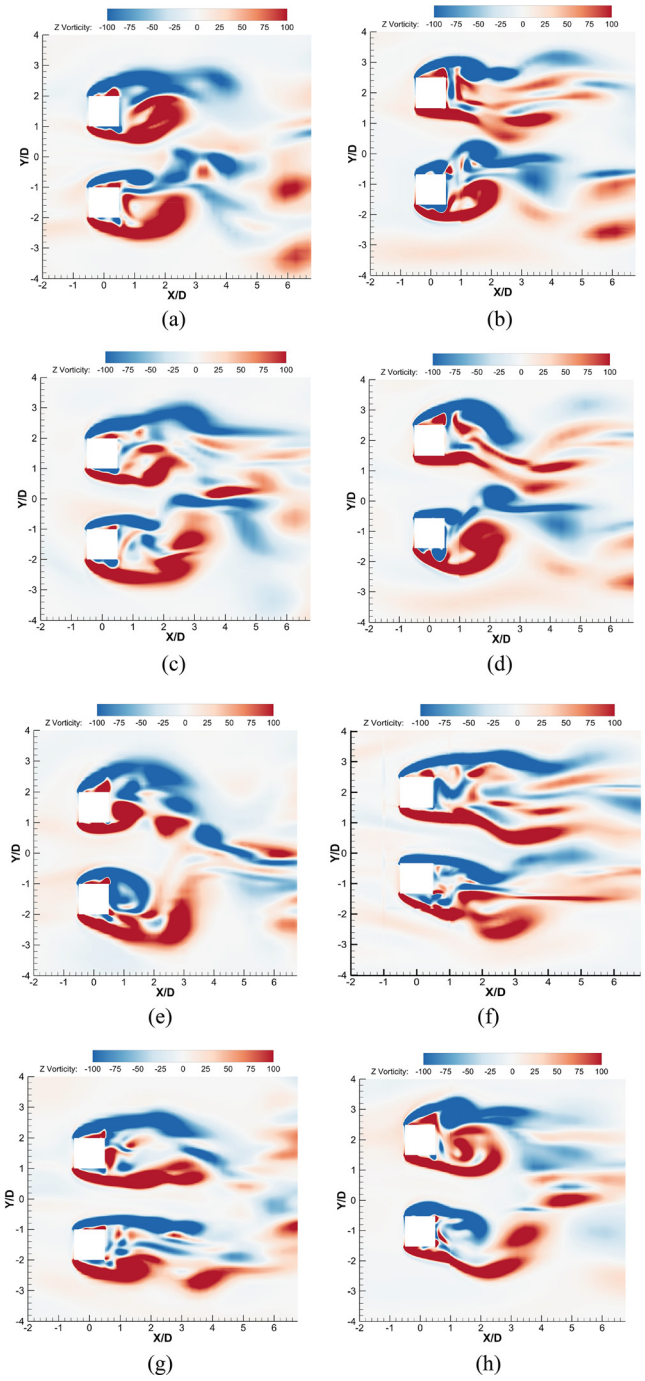

FIG. 21. Comparison of spanwise instantaneous vorticity between case 2 (stationary) and case 4 (vibration): (a) case 2 t_1, (b) case 4 t_1, (c) case 2 t_2, (d) case 4 t_2, (e) case 2 t_3, (f) case 4 t_3, (g) case 2 t_4, and (h) case 4 t_4.

that as the spacing between the side-by-side square prisms increases, the velocity at the gap decreases slightly. Compared with the instantaneous vorticity at 2D spacing, the shear layer shifts from being tightly adjacent to the inner sides of the structures to being a certain distance away, and the separation bubble gradually increases. However, it is still observed that the thickness of the shear layer at the gap remains narrower than that at the outer side, and the narrow pipe effect still exists. Additionally, due to the sufficiently large distance between the two prisms, the gap flow can obtain sufficient streamwise momentum from the inflow and the flow over the top of the prisms to maintain stability. Therefore, the gap flow is not deflected under the 3D case.

For the side-by-side square prisms with a 3D spacing under forced vibration, it can be observed from Figs. 21(b), 21(d), 21(f), and 21(h) that when the interfering structure vibrates, it alters the separation distance between the prisms and increases the relative velocity between the fluid and the structures. This increase in relative velocity enhances the shear stress, leading to a thinner shear layer that is more prone to instability and vortex formation. At the same time, the gap flow intermittently deflects toward the interfering structure, interacting with the unstable vortices in the wake, and accelerates the momentum exchange between the wake and the gap flow, rapidly recovering the wake to a stable state. According to the research by Alam *et al.*,[20] for the case without vibration (case 2), the wake flows between the two prisms are symmetric, characterized as the CVS regime. For the vibrating case of case 4, the flow resembles the transition regime.

D. Instantaneous vortex structure in the wake

To further understand the spanwise instantaneous vorticity, Figs. 22–25 show the instantaneous vortex structure of the wake of cases 1–4. Figures 22 and 23 show the instantaneous vortex structure for cases 1 and 3, respectively. Case 1 represents stationary side-by-side square prisms with 2D spacing, while case 3 is forced vibration side-by-side square prisms with the same spacing. The t_1–t_4 indicate four different time instants. For the stationary side-by-side square prisms with 2D spacing (i.e., case 1), in the absence of vibration, the flow replenishing the gap between the prisms is observable due to the small spacing, increasing the streamwise momentum of the gap flow. This gap flow influences the wake region of the prisms, leading to irregular vortex-shedding behavior. It can be observed that the vortices shed from the inner side of the two prisms are coupled together, resulting in a more complex vortex structure. Additionally, the vortex structures of the two prisms exhibit a symmetrical form, which is mainly because when the fluid separates, the velocity outside the boundary layer slows down, implying an increase in pressure. The pressure upstream of the gap between the two prisms may be higher than the pressure near the gap, resulting in a pressure difference in the lateral direction of the two prisms. This pressure difference may be symmetrical with respect to the midpoint of the gap, suppressing antisymmetric vortex shedding and causing symmetrical flow behavior. For the side-by-side square prisms with 2D spacing under forced vibration (i.e., case 3), when the interfering structure vibrates, it causes an earlier separation point at its trailing edge, forming an hairpin vortex. The shedding frequency of the hairpin vortex generated by the interfering structure is significantly higher than the principal structure, resulting in the asymmetry of the vortex structure in the wake region. At the same time, the vibration of the interfering structure also affects the flow near its end, weakening the end effect so that the integrity of the hairpin vortex is compromised, resulting in the formation of more fragmented vortices. On the other hand, the vibration of the interfering structure, coupled with the three-dimensional effect, causes the downwash flow between the

28 November 2025 03:08:21

Published under an exclusive license by AIP Publishing

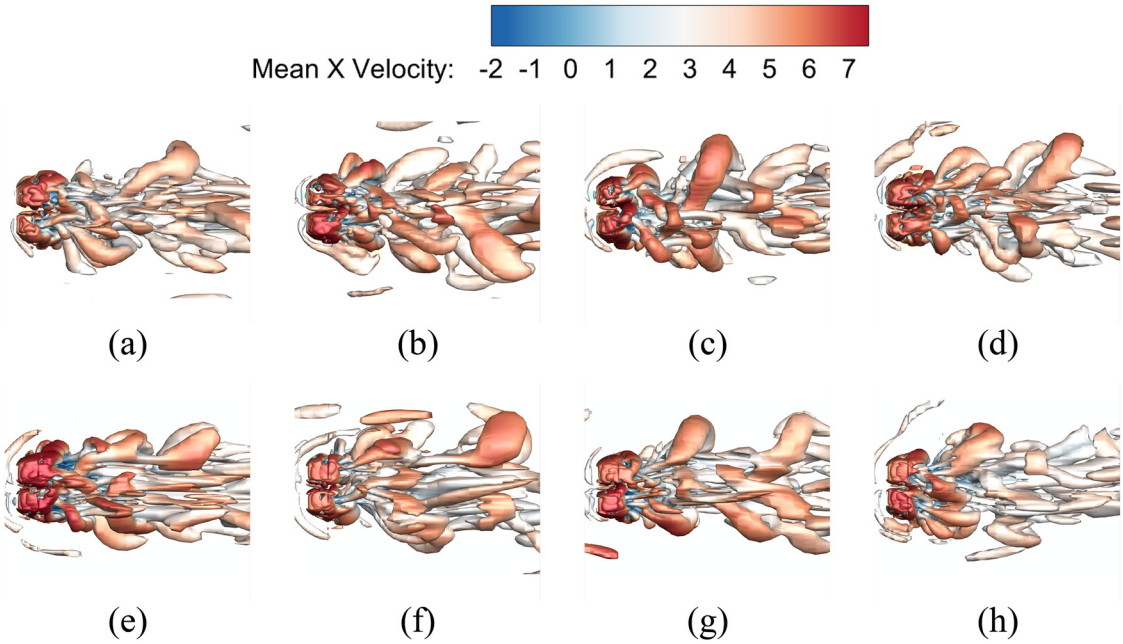

FIG. 22. Comparison of top view of instantaneous vortex structure between case 1 (stationary) and case 3 (vibration): (a) case 1 t_1, (b) case 1 t_2, (c) case 1 t_3, (d) case 1 t_4, (e) case 3 t_1, (f) case 3 t_2, (g) case 3 t_3, and (h) case 3 t_4.

prisms to become more complex, further increasing the complexity and instability of the flow.

Figure 24 presents a comparative top view of the instantaneous vortex structure for case 2 and case 4. In the absence of vibration (i.e., case 2), the instantaneous vortex structure in the wake region of the side-by-side square prisms exhibits a symmetrical distribution pattern. This symmetry arises because the spacing between the side-by-side square prisms is sufficiently large, the interference effect of the two prisms is weakened, reducing the interaction of vortex structures in the wake region, thus forming a symmetrical vortex structure. In the case of vibration (i.e., case 4), there is a notable change in the curvature of the shear layer of the interfering structure. Compared with the case without vibration, the curvature of the shear layer increases significantly, indicating that the separation point has moved upstream. This shift shortens the wake region width of the interfering structure. Observing cases 2 and 4 at moment t_1, it is evident that the vibration of the structure leads to a reduction in the thickness of the shear layer, consequently diminishing its influence in the crosswind direction.

Figure 25 compares the side view of the instantaneous vortex structure for cases 2 and 4. The observations reveal that for stationary side-by-side square prisms with a 3D spacing (i.e., case 2), the flow at the leading edge of the structures is blocked by the prisms, causing flow separation and forming an hairpin vortex structure with a certain curvature. These hairpin vortices, driven by the downwash flow and interacting with the gap flow, eventually lead to the dissipation and merging of the vortices. When the interfering structure vibrates (i.e.,

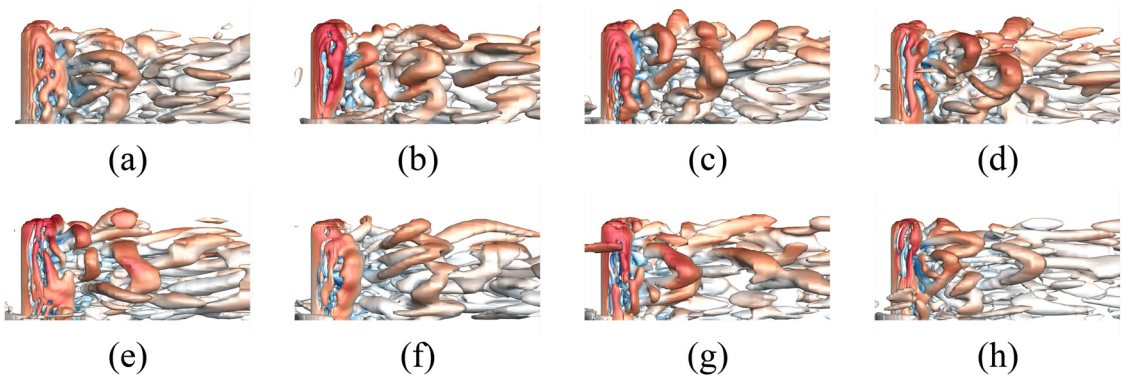

FIG. 23. Comparison of lateral view of instantaneous vortex structure between case 1 (stationary) and case 3 (vibration): (a) case 1 t_1, (b) case 1 t_2, (c) case 1 t_3, (d) case 1 t_4, (e) case 3 t_1, (f) case 3 t_2, (g) case 3 t_3, and (h) case 3 t_4.

28 November 2025 03:08:21

Published under an exclusive license by AIP Publishing

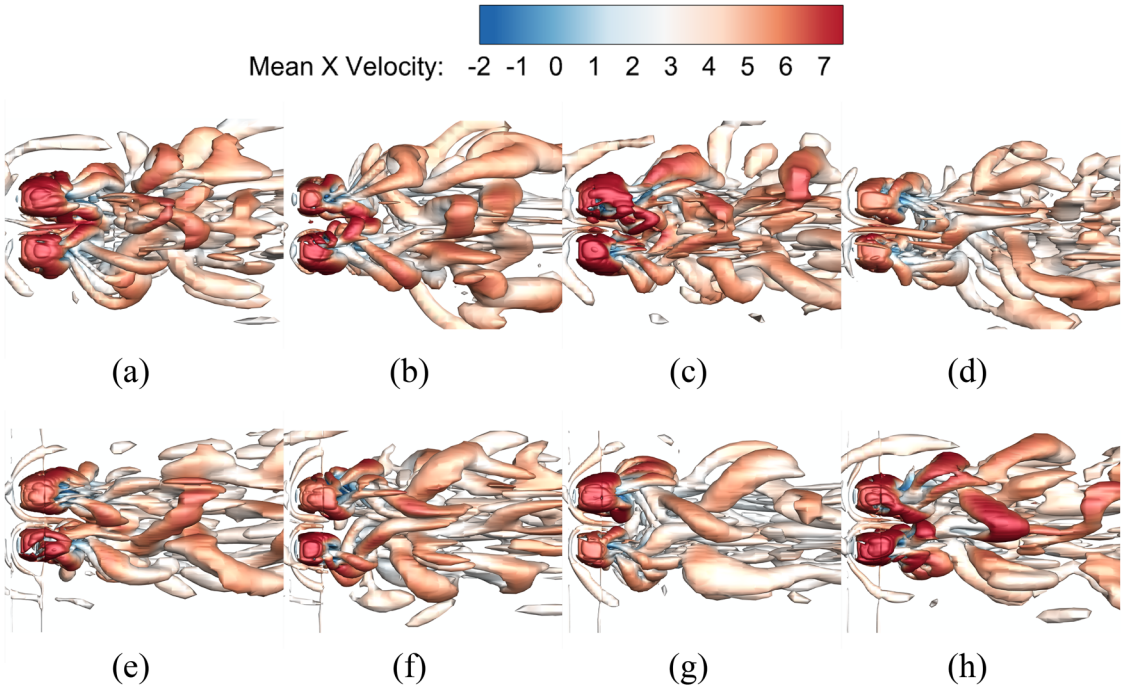

FIG. 24. Comparison of top view of instantaneous vortex structure between case 2 (stationary) and case 4 (vibration): (a) case 2 t_1, (b) case 2 t_2, (c) case 2 t_3, (d) case 2 t_4, (e) case 4 t_1, (f) case 4 t_2, (g) case 4 t_3, and (h) case 4 t_4.

case 4), the fluid dynamic behavior of the interfering structure changes significantly, mainly manifested in the following aspects: first, the vibration weakens the end effect of the interfering structure; second, the vibration disrupts the integrity of the axial vortices in the wake region of the interfering structure, resulting in the formation of more fragmented vortices. These findings are crucial for understanding the flow behavior of side-by-side square prisms and the influence mechanism of structural vibration on the flow field.

V. CONCLUDING REMARKS

This study utilizes NSRFG as the inlet turbulence generation for the finite-length side-by-side square prisms. Then, it conducts large eddy simulation of both rigid models and forced vibration models at various spacing. The study involves analyzing the aerodynamic characteristics of the side-by-side square prisms as well as the time-averaged streamlines, time-averaged wake vortex structures, spanwise instantaneous vorticity, and instantaneous vortex structure in the wake. This

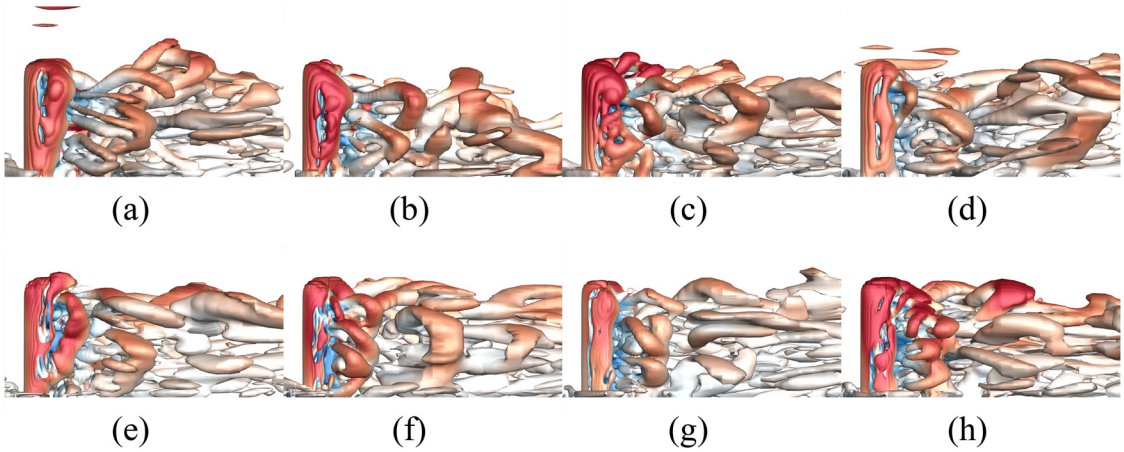

FIG. 25. Comparison of lateral view of instantaneous vortex structure between case 2 (stationary) and case 4 (vibration): (a) case 2 t_1, (b) case 2 t_2, (c) case 2 t_3, (d) case 2 t_4, (e) case 4 t_1, (f) case 4 t_2, (g) case 4 t_3, and (h) case 4 t_4.

28 November 2025 03:08:21

Published under an exclusive license by AIP Publishing

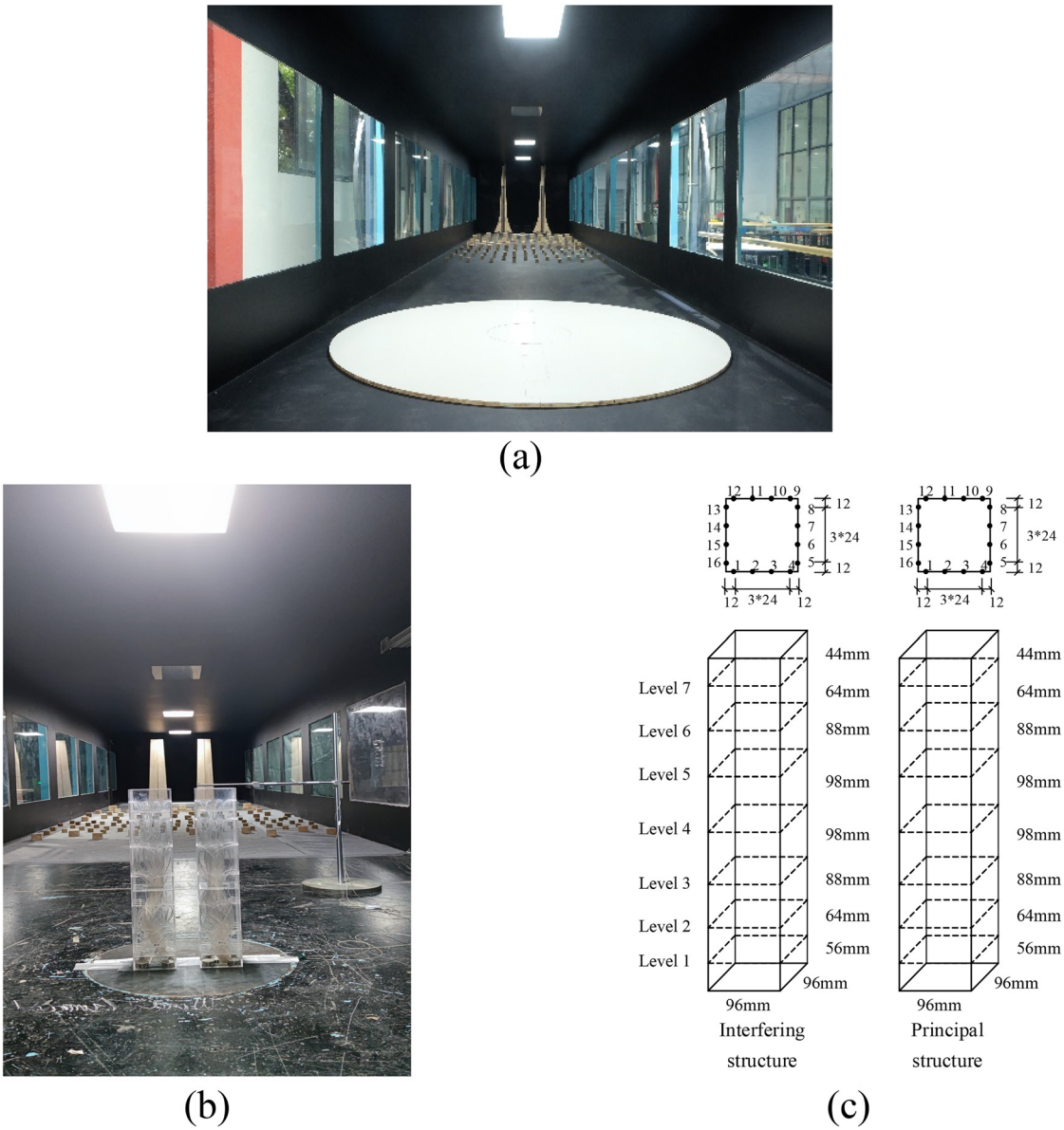

FIG 26. Details of the wind tunnel experiment: (a) inside direct flow wind tunnel laboratory of Chongqing University, (b) the side-by-side square prisms arrangement, and (c) the size of the test model and the locations of the pressure measurement points.

reveals the flow field morphology under vibration and varying spacing, establishing a relationship between aerodynamic characteristics and flow field phenomena. The main conclusions are as follows:

(1) The three-dimensional effect of the side-by-side square prisms effectively suppresses the deflection of the gap flow. The inflow and the flow at the top of the prism are induced to supplement the gap so that the gap flow has sufficient streamwise momentum and is difficult to deflect. At the same time, due to the three-dimensional effect, the flow on the upper part of the free end is drawn downward to form a downwash flow, while the flow at the base is drawn upward, creating an upwash flow.

(2) The narrow pipe effect accelerates the flow in the gap, leading to a reduction in the pressure coefficient at the gap of the side-by-side square prisms. Additionally, the narrow pipe effect causes the shear layer between the two prisms to narrow. The streamlines in the gap converge, reducing the spacing between them. This "squeezing" of the flow results in the congregation and inward compression of the time-averaged streamlines, elongation toward the rear, and changes in the position and extent of the wake vortices.

(3) Structural vibration increases the curvature of the interfering structure shear layer. In the case of the side-by-side square prisms with 2D spacing, the vortex separating from the trailing

28 November 2025 03:08:21

Published under an exclusive license by AIP Publishing

edge of the structure has sufficient lateral momentum. This induces the gap flow to deflect toward the interfering structure, significantly increasing the negative pressure on the leeward side of the interfering structure. At the same time, structural vibration weakens the end effect of the interfering structure. This destroys the integrity of the axial vortices in the wake, resulting in a more fragmented vortex formation.

(4) In the case of the side-by-side square prisms with 3D spacing, the narrow pipe effect is effectively weakened, the flow acceleration is relatively slowed down, and the constraining effect of vortex squeezing is also reduced. The time-averaged vortex structure becomes more symmetric, and the merged dipole vortex is also separated into a more independent vortex structure. The shear layer separating from the leading edge of the structure, instead of clinging closely to the inner sides of the structures, now maintains a certain distance from the sides. The separation bubbles gradually enlarge, and the instantaneous vorticity exhibits a symmetrical distribution pattern.

ACKNOWLEDGMENTS

The authors are grateful for the testing facility and the technical assistance provided by the CLP Power Wind/Wave Tunnel Facility at Chongqing University. The work is funded by the National Natural Science Foundation of China (NSFC) (Grant No. 51908090), the Fundamental Research Funds for the Central Universities (Fundamental Research Fund for the Central Universities) (Project Nos. 2022CDJXY-016 and 2023CDJXY030), the Natural Science Foundation of Chongqing Municipality (Project No. 2022NSCQ-JQX2377), the Key project of Technological Innovation and Application Development in Chongqing (Grant Nos. CSTB2022TIAD-KPX0145 and CSTB2022TIADKPX0142), and the National Foreign Specialist Platforms and Projects, (Award/Contract No. DL2023165002L), the National Natural Science Foundation Innovation Group Project of China (Grant No. 52221002), and the 111 project of the Ministry of Education and the Bureau of Foreign Experts of China (No. B18062).

AUTHOR DECLARATIONS

Conflict of Interest

The authors have no conflicts to disclose.

Author Contributions

Zengshun Chen: Conceptualization (equal); Funding acquisition (equal); Project administration (equal); Resources (equal); Supervision (equal). **Tengda Guan:** Methodology (equal); Software (equal);

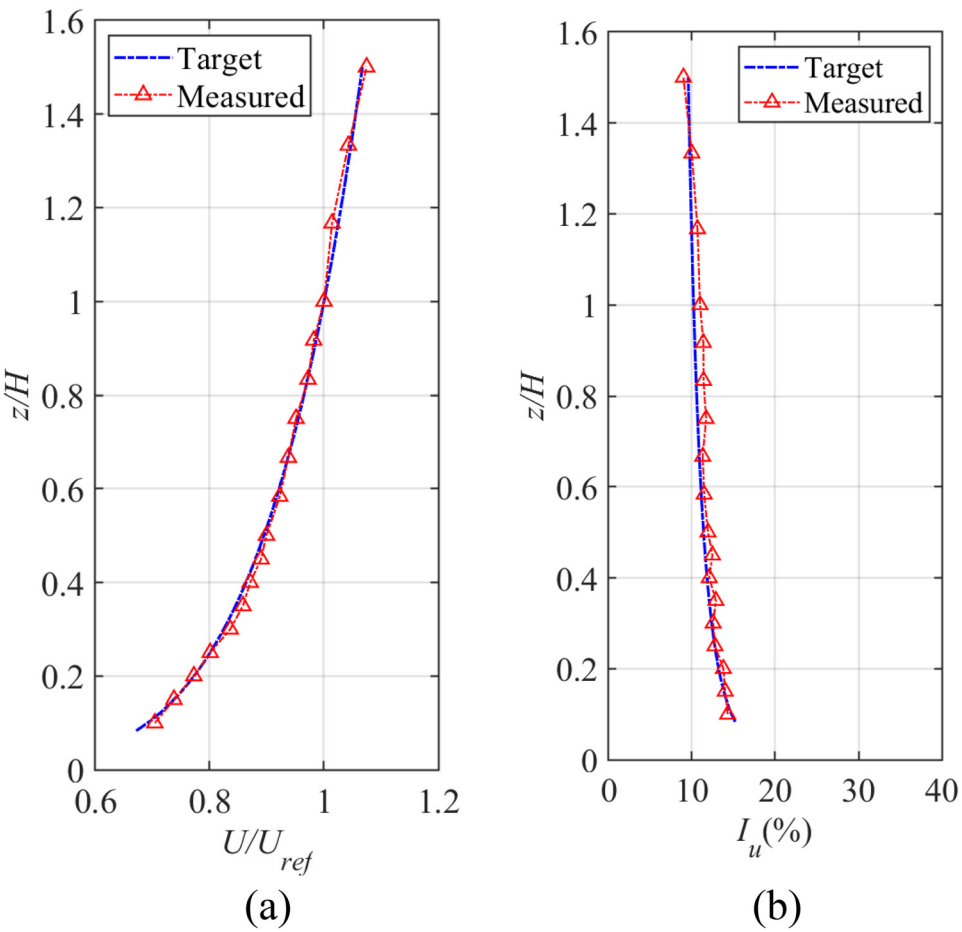

FIG 27. Wind field validation of the wind tunnel experiment: (a) velocity profile and (b) turbulence intensity.

28 November 2025 03:08:21

Published under an exclusive license by AIP Publishing

Validation (equal); Visualization (equal); Writing – original draft (equal); Writing – review & editing (equal). **Likai Zhang:** Formal analysis (equal); Investigation (equal); Methodology (equal); Software (equal); Supervision (equal); Visualization (equal); Writing – original draft (equal); Writing – review & editing (equal). **Sunwei Li:** Conceptualization (equal); Funding acquisition (equal); Investigation (equal); Project administration (equal); Supervision (equal). **Bubryur Kim:** Conceptualization (equal); Formal analysis (equal); Project administration (equal); Resources (equal); Supervision (equal). **Yemeng Xu:** Conceptualization (equal); Formal analysis (equal); Funding acquisition (equal); Methodology (equal); Software (equal); Supervision (equal); Validation (equal). **Yunfei Fu:** Conceptualization (equal); Formal analysis (equal); Methodology (equal); Project administration (equal); Resources (equal); Supervision (equal). **Cruz Y. Li:** Conceptualization (equal); Formal analysis (equal); Investigation (equal); Methodology (equal); Project administration (equal); Resources (equal); Supervision (equal).

DATA AVAILABILITY

The data that support the findings of this study are available from the corresponding author upon reasonable request.

APPENDIX: VALIDATION OF WIND TUNNEL EXPERIMENT

Figure 26 displays the details of the wind tunnel experiment, where (a) is the inside direct flow wind tunnel laboratory of Chongqing University, (b) is the figure of the side-by-side square prisms in the wind tunnel, and (c) is the size of the test model and the locations of the pressure measurement points. Figure 27 shows the wind field validation of the wind tunnel experiment, where (a) shows the velocity profile and (b) shows the turbulence intensity.

REFERENCES

[1] S. Nilsson, "Advanced fluid-structure interaction modelling and simulation for aerospace applications," Chalmers Tekniska Hogskola (Sweden).

[2] R. A. Febrianto, S. Hadi, R. L. L. G. Hidayat, D. M. Bae, B. Cao, and A. R. Prabowo, "Implementation of fluid-structure interaction (FSI) in marine design: Calculation review on hull structures," AIP Conf. Proc. **2674**, 030026 (2023).

[3] C. Feng, G. Fu, and M. Gu, "Numerical simulation of wind veering effects on aeroelastic responses of thousand-meter-scale super high-rise buildings," J. Build. Eng. **46**, 103790 (2022).

[4] Y. Sun, Z. Li, X. Sun, N. Su, and S. Peng, "Interference effects between two tall chimneys on wind loads and dynamic responses," J. Wind Eng. Ind. Aerodyn. **206**, 104227 (2020).

[5] A. Flaga, A. Kocoń, R. Kłaput, and G. Bosak, "The environmental effects of aerodynamic interference between two closely positioned irregular high buildings," J. Wind Eng. Ind. Aerodyn. **180**, 276–287 (2018).

[6] X. Yu, Z. Xie, and M. Gu, "Interference effects between two tall buildings with different section sizes on wind-induced acceleration," J. Wind Eng. Ind. Aerodyn. **182**, 16–26 (2018).

[7] M. Macháček, S. Urushadze, S. Pospíšil, A. Trush, and M. Pirner, "Aerodynamic interference of wind flow around three cylindrical bodies with surface roughness," MATEC Web Conf. **313**, 00051 (2020).

[8] R. Rajora, S. V. Veeravalli, and S. Ahmad, "Aerodynamic interference of straight and tapered cylinder pairs near the first critical wind speed," J. Wind Eng. Ind. Aerodyn. **201**, 104171 (2020).

[9] J. Chen, Y. Quan, and M. Gu, "Aerodynamic interference effects of a proposed super high-rise building on the aerodynamic forces and responses of an existing building," J. Wind Eng. Ind. Aerodyn. **206**, 104312 (2020).

[10] T. G. Mara, B. K. Terry, T. C. E. Ho, and N. Isyumov, "Aerodynamic and peak response interference factors for an upstream square building of identical height," J. Wind Eng. Ind. Aerodyn. **133**, 200–210 (2014).

[11] H. Zhao and M. Zhao, "Effect of rounded corners on flow-induced vibration of a square cylinder at a low Reynolds number of 200," Ocean Eng. **188**, 106263 (2019).

[12] S. Sen, "Wake modes of a freely vibrating square cylinder," Phys. Fluids **34**(5), 053601 (2022).

[13] C. M. Ma, Y. Z. Liu, Q. S. Li, and H. L. Liao, "Prediction and explanation of the aeroelastic behavior of a square-section cylinder via forced vibration," J. Wind Eng. Ind. Aerodyn. **176**, 78–86 (2018).

[14] T. P. Miyanawala and R. K. Jaiman, "Self-sustaining turbulent wake characteristics in fluid–structure interaction of a square cylinder," J. Fluids Struct. **77**, 80–101 (2018).

[15] C. Y. Li, Z. Chen, T. K. T. Tse, A. U. Weerasuriya, X. Zhang, Y. Fu, and X. Lin, "Establishing direct phenomenological connections between fluid and structure by the Koopman-Linearly Time-Invariant analysis," Phys. Fluids **33**(12), 121707 (2021).

[16] C. Y. Li, Z. Chen, X. Lin, A. U. Weerasuriya, X. Zhang, Y. Fu, and T. K. T. Tse, "The linear-time-invariance notion of the Koopman analysis: The architecture, practical rendering on the prism wake, and fluid-structure association," Phys. Fluids **34**(12), 125136 (2022).

[17] H. K. Jang, C. E. Ozdemir, J.-H. Liang, and M. Tyagi, "Oscillatory flow around a vertical wall-mounted cylinder: Dynamic mode decomposition," Phys. Fluids **33**(2), 025113 (2021).

[18] A. Sau, T.-W. Hsu, and S.-H. Ou, "Three-dimensional evolution of vortical structures and associated flow bifurcations in the wake of two side-by-side square cylinders," Phys. Fluids **19**(8), 084105 (2007).

[19] S. C. Yen and J. H. Liu, "Wake flow behind two side-by-side square cylinders," Int. J. Heat Fluid Flow **32**(1), 41–51 (2011).

[20] M. M. Alam, Y. Zhou, and X. W. Wang, "The wake of two side-by-side square cylinders," J. Fluid Mech. **669**, 432–471 (2011).

[21] S. J. Lee, G. S. Mun, Y. G. Park, and M. Y. Ha, "A numerical study on fluid flow around two side-by-side rectangular cylinders with different arrangements," J. Mech. Sci. Technol. **33**(7), 3289–3300 (2019).

[22] M. M. Alam and Y. Zhou, "Intrinsic features of flow around two side-by-side square cylinders," Phys. Fluids **25**(8), 085106 (2013).

[23] J. Mizushima and G. Hatsuda, "Nonlinear interactions between the two wakes behind a pair of square cylinders," J. Fluid Mech. **759**, 295–320 (2014).

[24] P. C. Lu, C. M. Cheng, and C. W. Cheng, "Aerodynamic forces on two stationary and oscillating square prisms in tandem and side by side arrangements," J. Chin. Inst. Eng. **21**(5), 535–546 (1998).

[25] B. Liu and R. K. Jaiman, "Interaction dynamics of gap flow with vortex-induced vibration in side-by-side cylinder arrangement," Phys. Fluids **28**(12), 127103 (2016).

[26] M. Z. Guan, R. K. Jaiman, K. Narendran, K. C. H. Wu, A. T. B. Lim, and C. W. Kang, "Fluid-structure interaction of combined and independent configurations of two side-by-side square cylinders at low Reynolds number," Int. J. Heat Fluid Flow **72**, 214–232 (2018).

[27] S. Kim and M. M. Alam, "Characteristics and suppression of flow-induced vibrations of two side-by-side circular cylinders," J. Fluids Struct. **54**, 629–642 (2015).

[28] W. Xu, H. Wu, M. Sha, and E. Wang, "Numerical study on the flow-induced vibrations of two elastically mounted side-by-side cylinders at subcritical Reynolds numbers," Appl. Ocean Res. **124**, 103191 (2022).

[29] A. Sohankar, M. Abbasi, M. Nili, F. Zafar, and M. Alam, "Flow around two finite side-by-side square cylinders," Mater. Res. **70**(5), 457–480 (2018).

[30] A. Sohankar, A. R. Bahmani, and M. R. Rastan, "An LES study of the wake flow dynamics and heat transfer characteristics of two side-by-side finite wall-mounted square cylinders," Ocean Eng. **266**, 113104 (2022).

[31] M. M. Zdravkovich, "Aerodynamics of two parallel circular cylinders of finite height at simulated high Reynolds numbers," J. Wind Eng. Ind. Aerodyn. **6**(1–2), 59–71 (1980).

[32] D. Bhamitipadi Suresh, E. J. Aju, and Y. Jin, "Turbulent boundary layer flow over two side-by-side wall-mounted cylinders: Wake characteristics and aerodynamic loads," Phys. Fluids **32**(11), 115104 (2020).

28 November 2025 03:08:21

Published under an exclusive license by AIP Publishing

[33]C. W. Park and S. J. Lee, "Flow structure around two finite circular cylinders located in an atmospheric boundary layer: Side-by-side arrangement," J. Fluids Struct. **17**(8), 1043–1058 (2003).
[34]P. Gousseau, B. Blocken, and G. J. F. Van Heijst, "Quality assessment of Large-Eddy Simulation of wind flow around a high-rise building: Validation and solution verification," Comput. Fluids **79**, 120–133 (2013).
[35]Y. Tominaga, A. Mochida, R. Yoshie, H. Kataoka, T. Nozu, M. Yoshikawa, and T. Shirasawa, "AIJ guidelines for practical applications of CFD to pedestrian wind environment around buildings," J. Wind Eng. Ind. Aerodyn. **96**(10–11), 1749–1761 (2008).
[36]Y. Yu, Y. Yang, and Z. Xie, "A new inflow turbulence generator for large eddy simulation evaluation of wind effects on a standard high-rise building," Build. Environ. **138**, 300–313 (2018).
[37]H. Aboshosha, A. Elshaer, G. T. Bitsuamlak, and A. El Damatty, "Consistent inflow turbulence generator for LES evaluation of wind-induced responses for tall buildings," J. Wind Eng. Ind. Aerodyn. **142**, 198–216 (2015).
[38]S. H. Huang, Q. S. Li, and J. R. Wu, "A general inflow turbulence generator for large eddy simulation," J. Wind Eng. Ind. Aerodyn. **98**(10–11), 600–617 (2010).
[39]M. Ricci, L. Patruno, I. Kalkman, S. De Miranda, and B. Blocken, "Towards LES as a design tool: Wind loads assessment on a high-rise building," J. Wind Eng. Ind. Aerodyn. **180**, 1–18 (2018).
[40]Z. Chen, Y. Wang, S. Wang, H. Huang, K. Yuan, S. Li, C. Y. Li, and Y. Xu, "Fluid–structure interaction on vibrating square prisms considering interference effects," Phys. Fluids **35**(12), 125111 (2023).
[41]I. B. Celik, Z. N. Cehreli, and I. Yavuz, "Index of resolution quality for large eddy simulations," J. Fluids Eng. **127**(5), 949–958 (2005).
[42]R. Vasaturo, I. Kalkman, B. Blocken, and P. J. V. Van Wesemael, "Large eddy simulation of the neutral atmospheric boundary layer: Performance evaluation of three inflow methods for terrains with different roughness," J. Wind Eng. Ind. Aerodyn. **173**, 241–261 (2018).
[43]N. S. Dhamankar, G. A. Blaisdell, and A. S. Lyrintzis, "Overview of turbulent inflow boundary conditions for large-eddy simulations," AIAA J. **56**(4), 1317–1334 (2018).
[44]Z. Chen, H. Huang, Y. Xu, K. T. Tse, B. Kim, and Y. Wang, "Unsteady aerodynamics on a tapered prism under forced excitation," Eng. Struct. **240**, 112387 (2021).
[45]Z. Chen, Y. Wang, S. Wang, H. Huang, K. T. Tse, C. Y. Li, and C. Lin, "Decoupling bi-directional fluid–structure interactions by the Koopman theory: Actualizing one-way subcases and the role of crosswind structure motion," Phys. Fluids **34**(9), 095103 (2022).
[46]Z. Chen, S. Li, L. Zhang, C. Yuan, Z. Zhao, Y. Wu, Y. Xu, and C. Y. Li, "Characteristics of aerodynamic interference and flow phenomenology around inclined square prisms," Phys. Fluids **35**(12), 125119 (2023).

28 November 2025 03:08:21

Published under an exclusive license by AIP Publishing